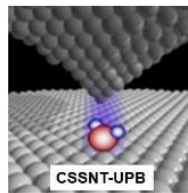**UNIVERSITY POLITEHNICA OF BUCHAREST**
DOCTORAL SCHOOL OF APPLIED SCIENCE

PhD THESIS - SUMMARY

SYNTHESIS AND CHARACTERIZATION OF
SEMICONDUCTOR NANOMATERIALS AND THIN FILMS

Author: Phys. Călin Constantin Moise
Supervisor: Prof. Dr.rer.nat. Marius Enăchescu

Bucharest, July 2022

UNIVERSITY POLITEHNICA OF BUCHAREST
DOCTORAL SCHOOL OF APPLIED SCIENCE

PhD THESIS - SUMMARY

SYNTHESIS AND CHARACTERIZATION OF SEMICONDUCTOR NANOMATERIALS AND THIN FILMS

Author: Phys. Călin Constantin Moise
Supervisor: Prof. Dr.rer.nat. Marius Enăchescu

Bucharest, July 2022

CONTENT

Keywords: Single-walled Carbon Nanotubes (SWCNTs), CuO Nanowires, Thin Films, Nanostructured GaN, Raman, XRD, AFM-PSD, Ellipsometry, SEM-EDX, TEM-EDX.

This summary presents the content of chapters 3-6 which represent the original contribution. The numbering of chapters, subchapters, figures, tables, equations and references corresponds to that of the thesis.

THE MOTIVATION OF THE TOPIC AND THE GENERAL PRESENTATION OF THE THESIS

The importance of semiconductor nanomaterials, the enormous steps taken in recent years to reduce the size of electronic devices, large-scale projects at European level to obtain 3 and 2 nm electronic nodes, technology already implemented for 7 nm and 4 nm technology, used very recently by Samsung in the field of 2022 generation mobile phones, they are clear proof of the worldwide interest in this field of science.

Semiconductor nanomaterials involve a reduction in physical volume, energy consumption and heat dissipation, which means an increase in efficiency. By nanostructuring a material, the atoms on its surface become the majority of those in the volume, so they dictate all physicochemical processes. In other words, a nanostructured semiconductor element can be designed for a certain type of application. A conclusive example is that of a very sensitive gas sensor that will become also selective.

The thesis is structured in seven chapters, as follows:

Chapters 1 and 2 contain theoretical and technical information. These introductory chapters describe in detail the performance and operation of the equipment used within CSSNT (Center for Surface Science and Nanotechnology): the reactor for the synthesis of carbon nanomaterials and the PLD-MBE ultra high vacuum deposition system (UHV) produced by SVTA - USA.

Chapters 3, 4, 5, 6 and 7 describe personal contributions. Given the complexity and diversity of the topics covered, each of these five chapters included an introductory subchapter, as well as a subchapter describing the experimental techniques used to investigate nanomaterials.

Chapter 3 deals with the coating of carbon fibers with single-walled carbon nanotubes (SWCNTs), in order to improve the performance of composites, by modifying the physical properties at

the fiber-resin interface. The fibers were coated with SWCNTs in the innovative CSSNT reactor at different temperatures. A 20% increase in shear strength was demonstrated for deposition obtained at 290 ° C.

In Chapter 4 we studied the growth process of CuO semiconductor nanowires by thermal oxidation of Cu, at temperatures close to the threshold temperature. Several experimental techniques have demonstrated the presence of copper nanoaggregates inside the Cu_2O phase and a theoretical model of the growth kinetics of nanowire groups has been proposed. The model fits the experimental data well and tests the saturation of the nanowire length at relatively short oxidation times (up to 40 minutes). The current-voltage (I-V) characteristic for an individual CuO nanowire with a diameter of 20 nm was also analyzed.

Chapter 5 presents the synthesis of SOI (silicon on insulator) layers made by laser ablation. For this purpose, a thin layer of TiO_2 was deposited on the Si substrate (100), at three target - substrate distances. A second thin layer of Si was deposited over this layer under the same conditions. Both deposited layers were investigated using AFM (Atomic Force Microscope) to find the optimal deposition distance. AFM data were processed and analyzed by PSD (Power Spectral Density). All the results of the experiments indicated that the layer deposited at 5 cm between the target and the substrate has the lowest spectral roughness. The samples were also analyzed by XRD (X-ray diffraction) highlighting the presence of the brookite phase for TiO_2 deposition. To measure the thickness of the TiO_2 layer, 26 nm, ellipsometry was involved.

Chapter 6 presents the nanostructuring of GaN wafers. Electrochemical etching has been successfully applied to achieve porous structures in crystalline GaN wafers. Pores were made using nitric and sulfuric acid. The possibility to achieve uniform pores in a much more environmentally friendly solution, namely water NaCl solution, has been demonstrated. There were differences in structuring depending on where the electrochemical attack begins, respectively attack on the Ga face or attack on the N face.

Chapter 7 presented some topics and investigations that are ongoing and are to be continued and published. The first topic is the synthesis by laser ablation (PLA) and the characterization of hollow carbon nano-onions (CNOs), with a large number of shells. A new method of dispersing CNOs in BSA has been successfully used. The second issue is the formation of uniform pores in InP wafers being investigated two types of wafers with different concentrations of free carriers. It was observed that at higher concentration of carriers the pores were 5 times finer than at low concentration. Electrochemical deposition of Ni nanoparticles has been successfully performed in larger pores.

The thesis ends with a list of experimental techniques learned by the doctoral student, the list of 17 ISI papers published by the author during his doctoral studies, of which 4 as first author, a book chapter also as first author and the summary table with indicators IF (total = 65), AIS (total 11.4) and SRI (total 26). A selection of international conferences at which the author had oral presentations is also included.

CHAPTERS ORIGINAL CONTRIBUTION:

3 Pulsed Laser Deposition of SWCNTs on Carbon Fibres: Effect of Deposition Temperature

3.4 Results

3.4.1 SWCNTs Characterization

Confocal micro-Raman spectroscopy was used for SWCNTs characterization. Raw material was collected from the edge of CF where the deposition temperature was 25 °C. In Figure 47 a), a typical Raman spectrum of SWCNTs acquired at room temperature is shown. It is well known that SWCNTs present a special fingerprint in Raman spectra, namely, the radial breathing mode (RBM) band on lower frequency, a disorder band called D band, and a graphitic G band at higher frequencies [20].

From the RBM band, the value of SWCNTs diameters can be determined via an empirical Equation (1) [21]. As can be seen in Figure 47 b, there are two peaks in RBM corresponding to SWCNTs diameters: 1.28 and 1.46 nm. G band splits into two bands called G- and G+ as shown in Figure 47 c; the ratio ID/IG = 0.07 indicates high quality of synthesized SWCNTs.

$$d = c_1/(\omega - c_2) \quad (1)$$

Where:
ω—frequency of vibrations in the radial direction [cm^{-1}]
c_1, c_2—constants [cm^{-1}];
c_1 = 215 [cm^{-1}] c_2 = 18 [cm^{-1}]
d—the diameter of the nanotubes [nm]
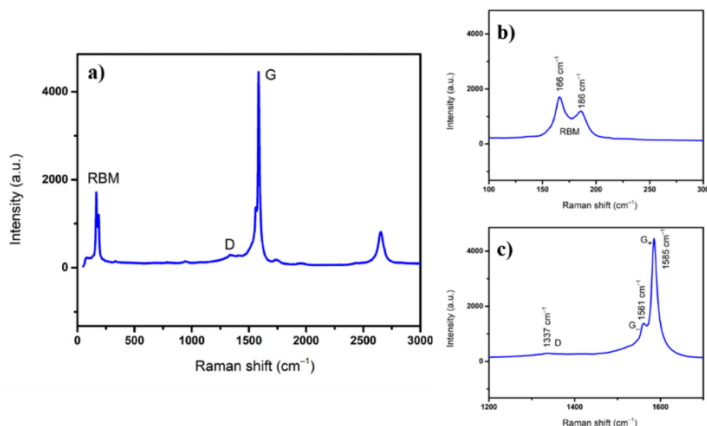
*Figure 47. (**a**) Typical Single Wall Carbon Nanotubes (SWCNTs) Raman spectra; (**b**) radial breathing mode (RBM) band and (**c**) D and G bands.*

HR-STEM images reveal SWCNTs with diameters around 1.3 nm, as shown in Figure 48. This is in good agreement with the values calculated via micro-Raman and in a previous study regarding the diameter distribution of SWCNTs, where an average diameter of 1.35 nm was found [22]. In conclusion, high quality SWCNTs are produced via PLD.
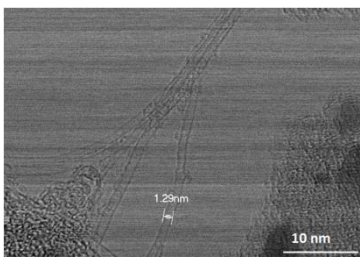
Figure 48. Measurement of individual SWCNT diameter by HR-STEM.

These high quality SWCNTs were deposited directly on the carbon fibres at different temperatures as described in sample preparation.

3.4.2   Fibres Covered by SWCNTs

In a preliminary study, desized fibres were placed directly onto the CF at different positions. A temperature gradient develops, such that the temperature is higher at its tip and lower at its base, as was

described in Sample Preparation. The fibres' positions on the Cold Finger are indicated in Figure 49 shown below.
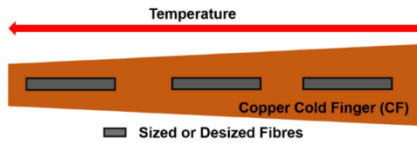
Figure 49. Schematics of the sample's positions on the Cold Finger for moderate temperature variation.

Temperature affects how SWCNTs are distributed along the fibres, as well as the SWCNTs growth rate. At low to mid temperatures, depending on the position of the fibre in the tow, a fine, rather even, covering of the fibre surface was obtained. In Figure 50, SWCNTs seem to arrange in a two-dimensional network connected by nodules. For a nucleation and growth mechanism, deposition probably started at the nodules, and extended in between due to the low growth rate at these rather low temperatures.
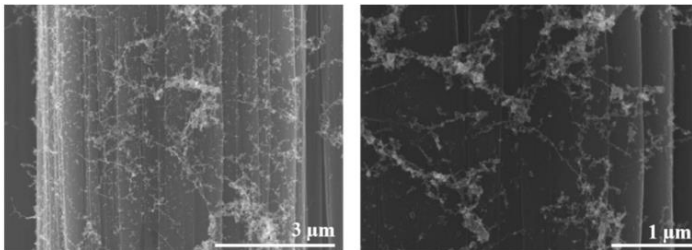
Figure 50. SWCNTs network on desized carbon fibres at low nodular growth rate.

As the deposition temperature increases, the nodules become larger and turn into clusters. The micrographs in Figure 51 reveal the effect of the deposition temperature. Low temperature resulted in uneven deposition with few desized fibres being coated, yet finer CNT nodules, 100 nm and less. Higher temperatures led to the formation of larger CNT nodules or clusters, in the order of 0.5 µm.
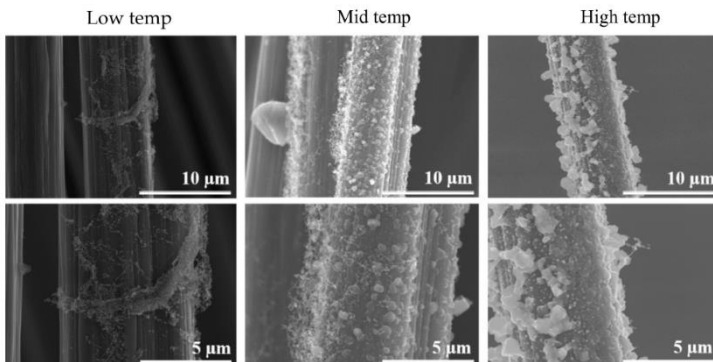
Figure 51. SWCNTs nodule and cluster formation on desized carbon fibres.

The carbon clusters were confirmed by EDX, typical results are given in Figure 52 and Table 4.
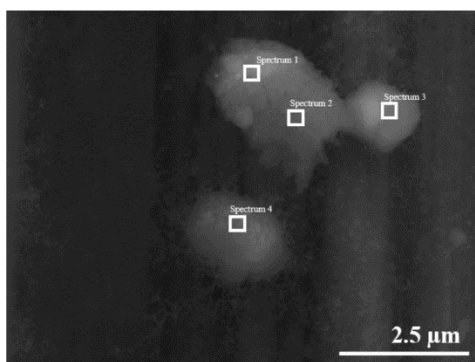
Figura 52. Determination of carbon clusters composition by EDX.

Table 4. Composition of the formed SWCNTs clusters.

Scheme 1.	Spectrum 1	Spectrum 2	Spectrum 3	Spectrum 4
C	96.23	95.70	96.05	97.67
O	3.77	4.30	3.95	2.33
Total	100	100	100	100

Statistics		C		O
Max		97.67		4.30
Min		95.70		2.33
Average		96.41		3.59
Standard Deviation		0.87		0.87

Next, a comparison was made between sized and desized fibres after exposure to mid-range temperatures. Figure 53 A shows that the desized fibres have a coarse, uneven pattern of SWCNTs clustering, whereas Figure 53 B shows that sized fibres were evenly coated with finer clusters.
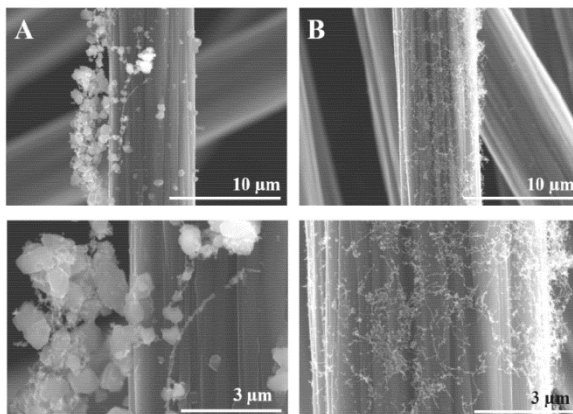
*Figure 53. Effect of sizing on PLD of SWCNTs on carbon fibres: (**A**) desized fibres, and (**B**) sized fibres.*

For a nucleation and growth mechanism, sizing seems to favour nucleation, while the desized fibres rather promote carbon cluster growth. Finally, desized fibres were exposed to several high temperatures by controlling the position while monitoring the temperature, as can be seen in Figure 54.
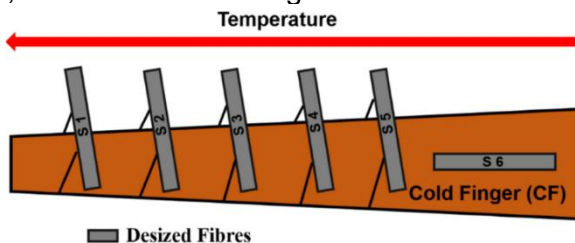
Figure 54. Schematics of the sample's positions on the Cold Finger for deposition at various temperatures.

This way, deposition took place at a wide range of temperatures, from 25 ∘C to 565 ∘C. Desized fibres are expected to withstand the relatively high exposure temperatures, while the sizing of commercial fibres would degrade and loose mass. Samples synthesized for this study are indexed in Table 5.

Table 5. Temperatures at which the analysed samples were obtained.

Sample Name	Temperature (°C)
Sample #1	565
Sample #2	390
Sample #3	290
Sample #4	200
Sample #5	100
Sample #6	25

SEM micrographs in Figure 55 show that the best deposition took place at 290 ∘C, on Sample 3, with a rather uniform coverage of the fibres. As can be seen, all the other samples, obtained at higher or lower temperatures, present some amount of SWCNTs on the fibres, but the coverage is not uniform. Deposition at 25 ∘C is much finer. Although uneven, a subtle coating of SWCNTs appears on extensive areas on the carbon fibres.
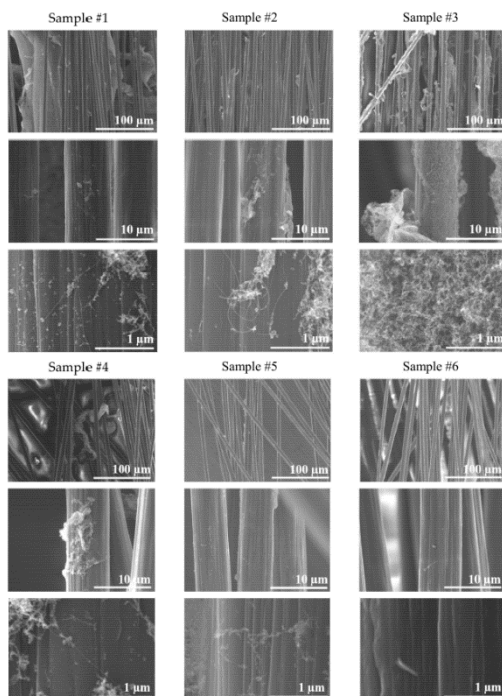
Figure 55. SEM micrographs of desized carbon fibres at various temperatures, PLD exposures, several magnifications.

Contact angles and surface free energies of the fibres are shown in Figure 56. The SFE calculation is based on the Owens–Wendt equation [23], which in turn is based on Young's equation [24]. It assumes smooth surfaces. We can elaborate on the validity of this equation for desized and SWCNTs coated fibres. The macroscopic, measurable contact angle depends not only on the thermodynamics of a smooth surface, but also on the effect of roughness. Desized carbon fibres were shown to exhibit larger surface areas than commercial fibres, by 10%. Desizing also appears to leave functional groups on the fibre surface [25]. Nevertheless, a SWCNTs network deposited on the carbon fibre surface increases the roughness at the micrometre to nanometre scale and may induce some porosity.
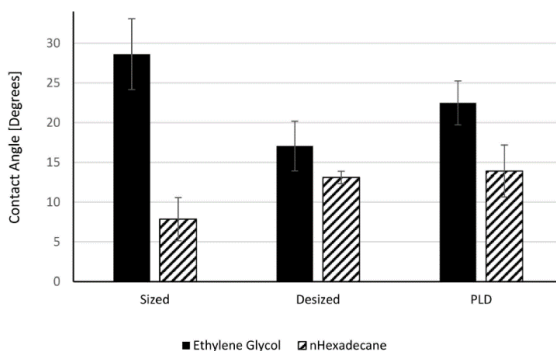
Figure 56. Contact angles of desized fibres after SWCNTs deposition.

Models like Wenzel's equation [26] and Cassie–Baxter's equation [27] have been proposed to take into consideration the effects of roughness and heterogeneities. Wenzel's model is usually applied for low contact angles ($\theta W < 90\circ$) and predicts a reduction of contact angle for "wetting" liquids due to surface roughness, whereas Cassie–Baxter's model is considered for large contact angles ($\theta CB > 90\circ$) and predicts an increase of contact angle for non-wetting liquids. With a polar liquid, desized and PLD samples show contact angles lower than the sized (commercial) fibres, and PLD samples show values somewhat higher than those of the desized fibres. This translates into a stronger polar component of the SFE of desized fibres in Figure 57, while the dispersive component remains unaffected. The results for the desized fibres can be explained by the increased surface area and the increased polarity. Thus, desized

fibres seem to follow the Wenzel model. However, an increased polarity of the PLD fibres cannot be explained by the composition of the coating, characterized in Table 4 by low oxygen content. The fine structure of the SWCNTs coating seems to increase the surface roughness and overall surface area of the fibre and may explain the reduction in contact angle of a polar liquid, compared to the commercial fibre. The opposite behaviour is seen with a nonpolar liquid. The increase in n-hexadecane contact angle indicates the oleophobic nature of the SWCNTs. SWCNTs are mostly carbon and, thus, hydrophobic and oleophobic, and their interaction with a nonpolar liquid leads to higher contact angles, as shown for n-hexadecane. Thus, in this case SWCNTs-coated carbon fibres seem to follow the Cassie–Baxter model, which predicts an increase in contact angle. We conclude that the wetting behaviour of SWCNTs-coated carbon fibres is complex, and either wetting or de-wetting may happen, depending on the morphology of the coating and the polarity of the wetting agent.
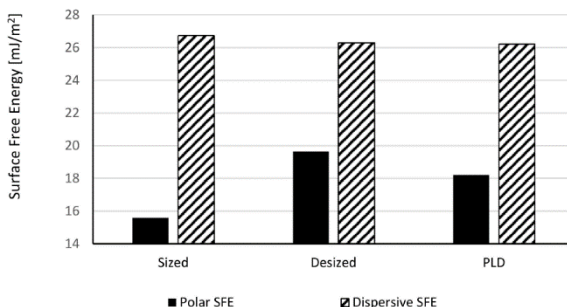
Figure 57. Surface Free Energy (SFE) of desized fibres after SWCNTs deposition.

Microdroplet pull-out tests of SWCNTs-coated fibres exhibit a bell-shaped dependence on temperature with a maximum at 290 ∘C. See Figure 58. Such behaviour can be explained by the nucleation and growth model. SWCNTs nucleation is more effective at the lower temperatures, but the SWCNT clusters are very small and the coating is uneven, leaving extensive surface areas uncovered. Intermediate temperatures allow for significant nucle- ation and growth, and a rather even coating is achieved. Higher exposure temperatures hamper growth, possibly due to cleavage of carbon–carbon linkages, and by 565 ∘C there is no deposition. SEM micrographs in Figure 55 seem to support this explanation.
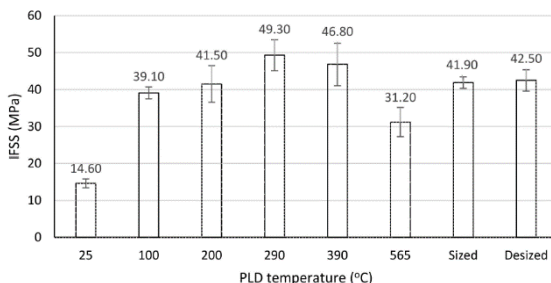
Figure 58. Interfacial shear strength (IFSS) of desized fibres PLD-treated at different temperatures. Values for sized (commercial) and desized fibres are shown for comparison.

Near 20% increase in Interfacial Shear Strength (IFSS) is obtained for deposition at 290 ◦C, compared to the sized (commercial) fibre. Although optimization was not done, these results show the potential to enhance the properties of the interface and increase the IFSS of carbon/epoxy composites. Interestingly, desizing did not affect the IFSS. Previous work indicates that desizing is not thorough, and certain functional groups, including urethane moieties, remain and contribute to matrix bonding [25].

Carbon fibres after exposure to the various temperatures and SWCNT deposition are shown to keep their original Tensile Strengths in Figure 59. This is due to the relatively low exposure temperatures enabled by this innovative PLD process. These conclusions are valid despite the relatively large standard deviations for the PLD-treated fibres, which clearly evolved during desizing.
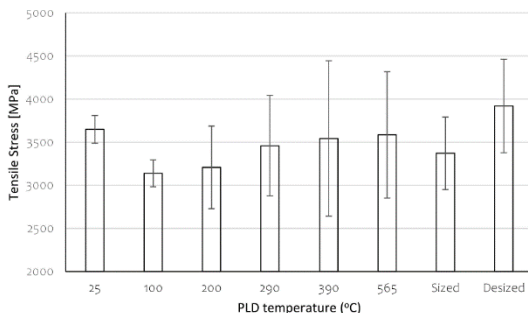
Figure 59. Tensile strength of PLD-treated fibres. Values for sized (commercial) and desized fibres are shown for comparison.

3.5   CONCLUSIONS

➢ SWCNTs were deposited on carbon fibres by PLD in a self-designed reactor. SWCNTs quality was proved by micro-Raman spectroscopy and HR-STEM.

➢ SEM images prove the successful deposition of SWCNTs onto carbon fibres at several temperatures. EDX was involved for chemical composition.

➢ Deposition of SWCNTs on the carbon fibres at certain conditions seems to reinforce the carbon/epoxy interface. In this study, a 20% increase in interfacial shear strength (IFSS) was observed by deposition at 290 ∘C, compared to the commercial carbon fibre sizing, without any effect on the tensile properties of the carbon fibres. SWCNTs deposition also affects the surface free energy and contact angles of liquids and may promote wetting or de-wetting depending on the polarity of the liquid.

4   On the growth of copper oxide nanowires by thermal oxidation near the threshold temperature at atmospheric pressure

4.4   Copper excess in non-stoichiometric Cu_2O phase

The scientific research on metals and alloys oxidation has a long tradition [16]. The best understanding is associated with the processes manifested at high temperatures, between 700 and 1000 ℃. Contrary, at low and intermediary temperatures, doubts and open questions remain, despite of many reported data. A complete understanding of the mechanisms of CuO NWs formation by copper oxidation, has not been reached [ ]. The control of CuO NWs growth is associated with critical features of the oxide layer and especially to the local configurations around the NWs. Cu ions emitted from the metallic substrate, due to the Kirkendall effect [ ], migrate by inter-grains diffusion to the surface where they react with oxygen. Passing through the Cu2O layer, to the top of CuO/Cu2O/Cu stacked structure, it is expected that copper atoms will be in excess especially at low oxidation temperatures. Accordingly, the local structure of the

cuprous oxide phase is populated with non-stoichiometric domains reached in copper.

The accurate determination of the copper content inside oxide layers using SEM - EDX is strongly affected by the proximity of the metallic substrate. The mitigation was found by using self-exfoliated NWs/CuO/Cu2O membranes produced by strain releasing during fast cooling of the annealed samples.

This interesting feature of copper oxidation in between 300 - 450 ℃ is associated with the non-stable mismatch of Cu2O/Cu region, where, under specific conditions, the oxide layer lifts off from the metallic substrate [26]. The induced thermal strain between Cu (cubic lattice, a=3.61 Å) and Cu2O (cubic lattice a=4.22 Å) is indicated by the difference in thermal expansion coefficients $2.3×10^{-5}$ K^{-1} and $0.3×10^{-5}$ K^{-1}, respectively [28].

Thick copper oxide sheets were prepared to be adequate mainly for XRD measurements. These results were corroborated with those obtained using SEM-EDX. The SEM micrograph shown in Fig. 60 a) represents the cross section of an exfoliated oxide sheet indicating the CuO/Cu2O phases. The on top CuO layer thickness is 2.1 µm, while the one of Cu2O is 6.1 µm.

The micrograph in Fig. 60 b) is taken above the CuO oxide layer showing a few CuO-NWs. Fig. 60 c) reveals the SEM micrograph of the opposite side of the oxide sheet, initially belonging to the interface with the metallic substrate. The topography is associated with the profile of the initial poly-crystalline copper surface, actually transformed into cuprous oxide. It is very dissimilar relative to porous CuO surface from the opposite face. The oxygen availability at the top CuO layer and the copper excess at the interface with the metallic poly-crystalline substrate makes the difference between the two faces of the oxide sheet. Fig.60 d) and e) give the SEM-EDX spectra collected from four regions of 1500x1500 nm^2 each one, taken from the both sides of the sample.
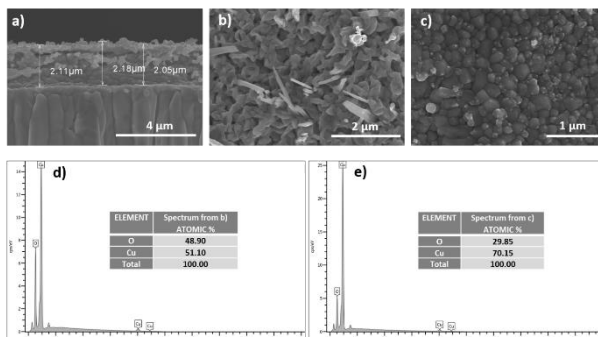
Figure 60. a) SEM cross section of thick exfoliated oxide membrane from copper foil substrate, oxidized in air, revealing the formation of CuO-Cu_2O stacked layers; b) Top view of the CuO phase, with CuO NWs c) Bottom side of the exfoliated oxide sheet, showing Cu_2O layer initially in contact with the copper substrate, d) SEM-EDX spectra of the upper side of the oxide membrane proving chemical content of CuO layer, e) SEM-EDX spectra of the bottom side of the oxide layer indicates Cu_2O phase containing an excess of Cu atoms of 10.45%.

Indeed, the spectra recorded from Fig. 60 b) shows an averaged chemical content of about 50.79 at.% Cu and 49.21 at.% O indicating a stoichiometry in agreement with CuO phase. The opposite scanned surface revealed in Fig. 60 c) has 70.13 at.% Cu and 29.85 at.% O which correspond to Cu_2O phase. The averaged excess of Cu atoms relative to stoichiometry, determined on different regions is in between 9.7 at.% and 19.1 at.%.

The detached oxide sheet from the copper foil facilitated structural characterization through XRD. Fig. 61 shows the X-Ray diffractogram of the same sample shown in Fig. 60. The Cu_2O phase belongs to cubic symmetry Pn-3m-224, a=b=c=4.2685 Å. The main diffraction features of cuprous oxide at 2θ as :36.4°, 42.3°, 61.3° and 73.5° corresponding to the atomic planes (111), (200), (220) and (311) are the same ones reported in [25]. The CuO pattern was indexed to a monoclinic structure C2/c-15, a=4.6883 Å, b=3.4229 Å and c=5.1319 Å   with the diffraction peaks at 2θ as: 35.5°, 38.7°, 48.9°, and 98.4° associated to the (002), (111), (20-2), and (223) planes.
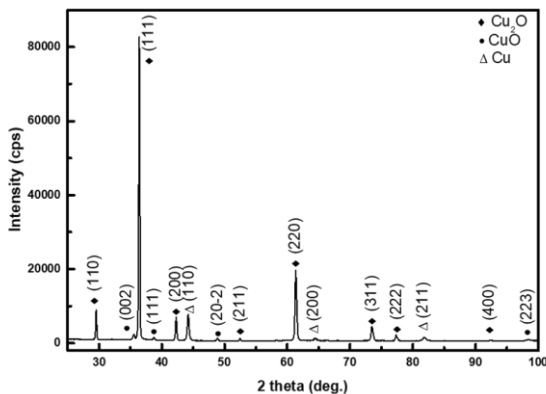
Figure 61. XRD diffractogram of detached thick CuO/Cu2O oxide sheet from copper foil substrate, the same as that in Fig. 1. Copper nanocrystals show diffraction lines for the planes of (110), (220) and (211), found inside the copper oxide host.

Nano-crystallites between 20-40 nm were determined according with the Scherrer's equation for the diffraction peaks at 2θ angles: 44.2°, 64.4° and 81.8° associated with the orientations (110), (200) and (211), respectively. EDX data of copper nanocrystals of 200-280 nm with cubic symmetry obtained by Scherrer's equation from XRD diffraction peaks appear at 2θ angles: 44.2°, 64.4° and 81.8° were associated to the (110), (200) and (211) planes, respectively. SEM-EDX data of the same exfoliated sample in Fig.1e), indicate that the copper aggregates belong to Cu_2O phase being embedded insight a metal-rich oxide, close to the copper-oxide interface.

The second type of the oxide sheets, shown in Fig. 62, are representative of samples used to investigate the kinetics of NWs growth by copper oxidation in between 30 min and 90 min at 340 ℃. Rare events of the random detachment of the oxide flakes take place especially in the case of samples oxidized at time intervals longer than 30 min. Such small CuO/Cu_2O samples with CuO NWs on top are valuable to measure accurately the excess of Cu content concerning with the oxide NWs growth. These samples were collected onto Au TEM grids covered with Lacey Carbon polymeric film. EDX spectra were recorded on the three selected regions of the sheet side initially as a part of the oxide-copper interface.

Element	Spectrum 3	Spectrum 4	Spectrum 5
	ATOMIC %	ATOMIC %	ATOMIC %
O	12.70	16.86	21.01
Cu	87.30	83.14	78.99
Total	100.00	100.00	100.00
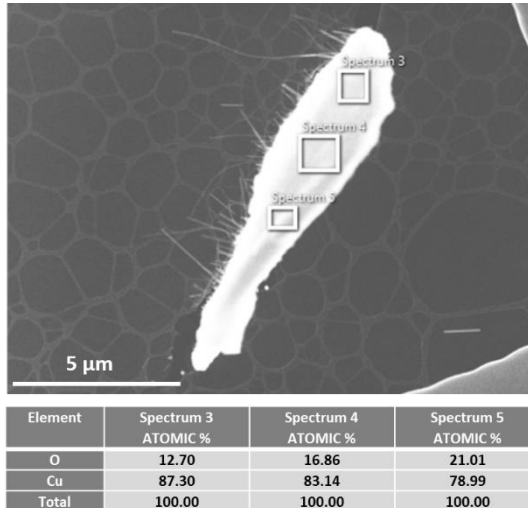
Figure 62. CuO/Cu$_2$O oxide flake with CuO NWs network on top, naturally exfoliated after copper foil oxidation of 60 min. at 340 ℃. EDX data acquired with STEM operated at 200 kV for samples collected on Au TEM grid. EDX spectra were recorded on the three selected regions of the sheet side initially as a part of the oxide-copper interface.

Metal-rich oxide Cu$_x$O has the following x values: 6.87, 4.43 and 3.76 corresponding to the three domains marked by rectangles. The gradient of copper concentration between the scanned regions shows heavily injected atoms from copper foil into the oxide, leading to an inhomogeneous interface. These thin oxide sheets have a larger copper content than the above thick samples annealed for a longer time. The distribution of the odd metallic atoms is the result of their transfer from substrate to the oxide bulk, followed by the inter-grains diffusion to the on top CuO layer, in respect to the concentration gradient. The oxygen reaction within the local sub-oxide phase leads to the growth of the overall oxide layer and determines CuO NWs to emerge throughout the pores of CuO.

Micro Raman Spectroscopy was used for the characterization of the thin oxide layer obtained after short-time annealing in air at 320 - 340 ℃ of copper foil. The inelastic scattering peaks of photons associated with Cu$_2$O and CuO single crystals, correspond to the selection rules linked to symmetry. Lattice defects, change the local symmetry, with consequences on activating some forbidden transitions. Starting from these general facts we used micro-Raman

technique to find more details about defects associated with extra copper content in metal-rich oxide.

Fig. 63 shows the Raman spectra of copper foils annealed as isochronal oxidation at 340 °C for 5, 20 and 30 min. The lines assigned to the CuO phase are: 298 (A_g), 340 (B_g) and 632 cm^{-1} (B_g) [29,30] being indicated by "#" symbol. The associated frequencies to Cu_2O were marked with circles. The most intense line at 214.9 cm^{-1} is also found in Cu_2O mono-crystal being the second overtone of that at 106.9 cm^{-1} [23,31]. The vibration at 145.6 cm^{-1}, forbidden in mono-crystalline Cu_2O, shows remarkable intensity due to a symmetry violation by incorporated defects into the oxide lattice [32]. The assignation of this line to structural defects in Cu_2O has been demonstrated by using ionic implantation [31]. The intensity of this line shows a systematic increase versus defects concentration up to the formation of amorphous islands in crystalline Cu_2O.

The spectral features in between 400 cm^{-1} and 550 cm^{-1} have been assigned to the amorphous phase Cu_xO with x>2 [33]. The lines at 298 cm^{-1} and 346 cm^{-1} increase in amplitude as a result of CuO layer growth on the samples surface. This observation agrees with reference [25] reporting on Raman spectra of oxidized copper for one hour in air at 100-400 °C. Contrary, the resonances associated with Cu_2O defects at 214, 145, 106, 400, and 550 cm^{-1} decrease their intensities with oxidation time.
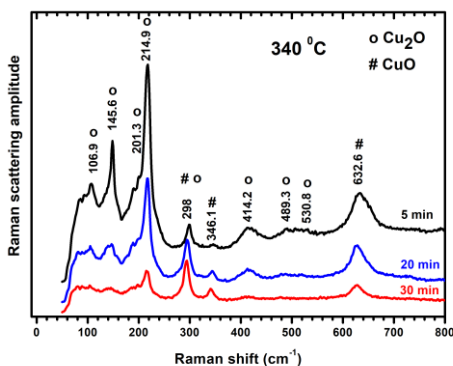
Figure 63. Raman spectra of Cu foil oxidized in air at 340 °C for 5, 20, and 30 min.

Considering that the majority of the defects were associated with the odd copper atoms inside in Cu_xO x>2, the above finding

seems to correlate with the difference of the copper amount in thick relative to thin oxide sheets, determined by SEM-EDX (Fig. 60 and Fig. 62). Unfortunately, accurate determinations of the defect population in Cu_2O cannot be simply extracted from micro-Raman spectra. The difficulty is associated with the modification of photons flux transmitted to the bottom Cu_2O layer, due to the increased thickness of on top cupric oxide. The similar behaviour of the same resonances has been reported in [25], associated to the different thickness of the on top CuO layer.

4.5   Temperature threshold of CuO NWs network formation

One goal of this study is to look inside the kinetics of CuO NWs close to the threshold temperature. The onset of nanowires network formation for isochron copper oxidation of 60 minutes is revealed by SEM micrographs in Fig. 64. At low temperature, the sample oxidized at 200 ℃ (Fig. 64a) shows only oxide grains of 40-67 nm in diameter. The grains become of large dimensions by fusing in clusters with diameters ranging between 67 nm up to 200 nm as copper oxidation goes to 250 ℃ (Fig. 64b).

Despite the fact that we are using hot plate instead tube furnace as the study reported by Hilman [25], the emerging of the tiny needles as the precursor of CuO-NWs was observed just as the same temperature of 250 ℃. This agreement shows that activation of the NWs growth does mainly depend on temperature. The dynamics of further growth of the nanowires become more dependent on experimental conditions.

Some isolated NWs already reached about one micron in length from the most reacting sites. Further increasing of oxidation temperature to 300 ℃ (Fig. 64c) determines the fusion of the nearest neighbouring grains into crystallites of 300-700 nm.
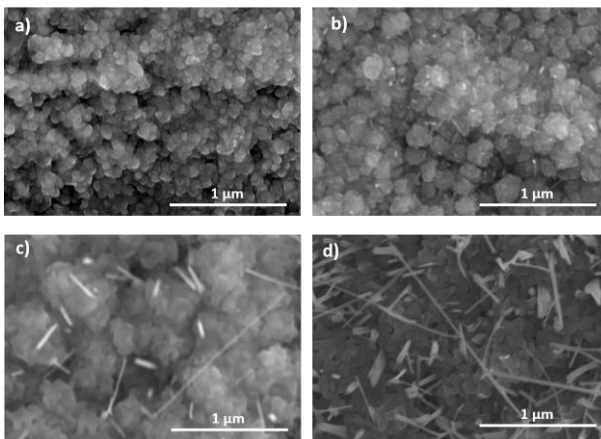
Figure 64. SEM micrographs on copper foils after 60 minutes of isochronal oxidation at different temperatures, seeking for the onset of CuO NWs network formation at a) 200 ℃; b) 250 ℃; c) 300 ℃; d) 350 ℃. The adequate temperature belongs to the interval 310 ℃ - 350 ℃.

The NWs network is still missing, but isolated groups are observed [34]. Medium population of CuO NWs emerges from the surface oxide after an hour of oxidation above 320 ℃, as other authors found [25,35]. In Fig. 64d) the SEM micrograph shows the surface morphology of the sample oxidized at 350 ℃. The CuO NWs network formation appears together with a visible change of CuO surface topography, from grainy structure to porous one, looking like a coverage of overlapped leaves. Therefore, the porous CuO surface layer observed to appear in between 300 ℃ and 350 ℃ should be considered to assist the transition from isolated NWs in the micrometre range to a medium density network at oxidation time of 60 minutes. The striking proof is based on SEM investigations on many samples oxidized in air above 320 ℃. Regarding the threshold temperature, it can be defined as that required to initiate the formation of CuO NWs precursor at 250 ℃ as shown Fig.5b) being confirmed by Hilman [25]. On the other hand, at 310 ℃, a specific patterning of CuO assists the formation of NWs network. Thus, we considered 310 ℃ as being representative for NWs network onset, triggered by specific CuO surface morphology. In conclusion we chose 320 - 340 ℃ as the adequate temperature for a study on the kinetic of the NWs growth at low rates in small or medium density network relative to copper oxidation time up to 60 min.

4.6 The kinetics of the CuO NWs growth

The unsatisfying understanding of the growth mechanisms at low temperature shadowed by the large non-homogeneity on large copper oxide surface almost cancels the advantages of the easiest way to get CuO NWs by thermal oxidation for the benefit of nanotechnology. The lack of an in-situ approach for the investigation of oxide NWs growth at atmospheric pressure imposes statistical analysis. The monitoring of the network of CuO NWs has been done by using one sample for each oxidation time interval, corresponding to a fixed temperature.

The micrographs in Fig. 65, represent the behaviour of the NWs population versus time obtained after Cu foil oxidation of 3, 20, 40 and 60 minutes, respectively, at 340 ℃. Fig. 65 reveals that after about 20 minutes of oxidation, the on top CuO layer looks like coverage of stacked leaves.
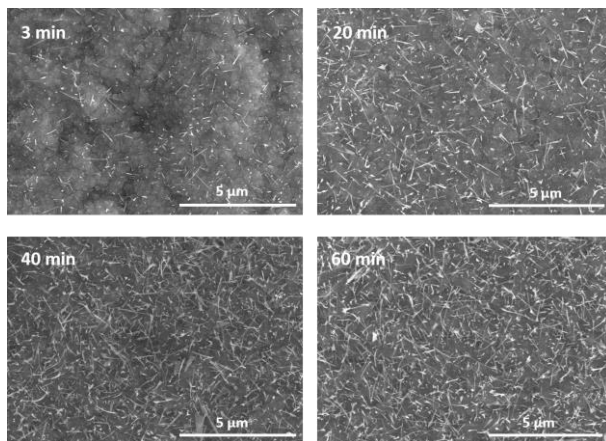
Figure 65. Oxidized samples at 340 ℃ for 3, 20, 40 and 60 min.

Fig. 66a) shows the average length of CuO NWs versus oxidation time ranging from 3 to 90 minutes at 320 ℃ and 340 ℃. The data were collected by SEM micrographs analysis taken for isothermal oxidized samples at time intervals represented on the abscissa. The curves are presented to guide the eyes. The early saturation in between 10 min up to 40 min is unexpected regarding

the previous results on the evolution of the NWs and of their network [25,35-37].

The established growth mechanism controlled by Cu ions diffusion on the NWs walls from the bottom to the top implies a parabolic low for the time dependence of their length [37]. The decrease of the slope in this case take place at longer time than in our results shown in Fig. 66a). In reference [25], Hilman reports the long-time behaviour in the same temperature range with saturation above two hours of oxidation at 300 ℃. Thus, the early saturation we have founded near the threshold temperature of CuO-NWs network formation by copper oxidation, required a different explanation. It is interesting to mention that the same early limitation of NWs growth in time has been observed in the case of copper nano-powder [38]. The plateau disappears in the case of oxidation above 360 ℃ or for oxidation time longer than 40 min. Being an oxidation process in air on hot plate, the statistic approach remains the only way to have insight into this matter. The drawbacks can be attenuated by considering the variation of NWs concentration $\Delta C(t)$, corresponding to a time interval Δt, divided by the NWs concentration $(\Delta C(t)/C(t))$, being used to represent the behaviour of the NWs population versus oxidation time.
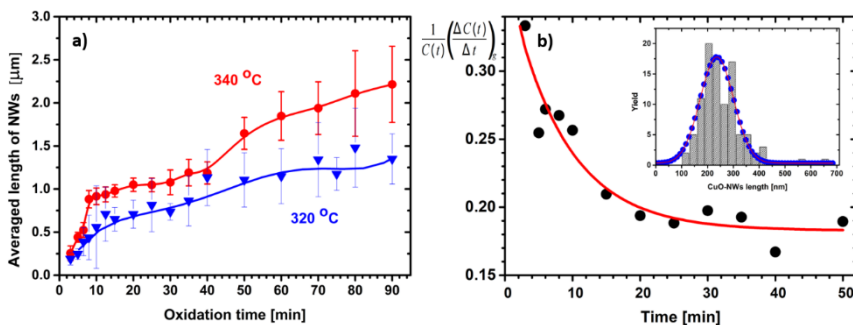
*Figure 66. a) The average length of CuO NWs versus copper oxidation time ranging from 4 to 90 minutes at 320 ℃ and 340 ℃. The data were collected by SEM micrographs analysis taken for isothermal oxidized samples at time intervals represented on the abscise. The curves are presented to guide the eye. b) Data extracted as C(t) and ΔC(t)/Δt from SEM micrographs of CuO NWs networks built by Cu foil oxidation at 340 ℃. The vertical axis represents the values given by 1/C(t)*ΔC(t)/Δt. The oxidation time is given on the abscissa. Inset b) Statistics on CuO NWs length after 3 minutes oxidation (considered as time window Δt in text) of poly-crystalline copper foil at 340 ℃ in air.*

SEM micrographs as those shown in Fig. 6 are used to determine $\Delta C(t)/C(t)$ for each oxidation time "t" corresponding to the samples prepared between 3 and 50 min. $\Delta C(t)$ can be estimated by counting the number of the CuO NWs per unit surface during the time window Δt, at the end of each sample oxidation, that means in between $t-\Delta t$ and t. This category of NWs can be identified looking at their length which is lower than 233.5 nm. This category of NWs can be identified considering their length corresponding to statistical distribution given in the inset of Fig. 66b), resulted after the copper foil oxidation of 3 min, assessed as the time window Δt. The error of time interval is estimated to 7.3% relative to the period necessary for thermal equilibrium of the sample on hot plate, and the time for its manipulation.

The number of the NWs emerged during the last 3 min of oxidation can be counted on any sample oxidized in the same conditions as the number of those having the length up to two times the average value 233.5 nm being associated with the Gaussian distribution symmetry of the inset in Fig. 66b). Fig. 66b) shows the graph of the ratio between the measured emerging rate $R=\Delta C(t)/\Delta t$ and the concentration of the oxide nanowires $(1/C(t)*\Delta C(t)/\Delta t)$ versus oxidation time at 340 ℃. The obtained values are well described by an exponential decay in time as that given in expression (1):

$$\frac{1}{C(t)}\left(\frac{\Delta C(t)}{\Delta t}\right) = ae^{-t/\tau} + b \tag{1}$$

Optimization leads to: a=0.193 +/- 0.031 s^{-1}
b=0.183 +/- 0.009 s^{-1}
τ =8.217 +/- 2.34 min

The physical meaning of this finding is just incorporated inside relation (1) that leads to specific correlation between the emerging rate and the concentration of CuO NWs versus time shown below. In fact, these data associated to R(t) gives an apparent value of the increasing rate of CuO-NWs. The evolution of CuO NWs population is marked by a continuous emerging of NWs and simultaneously by their incorporation inside of the growing copper oxide. The last process is linked to the tendency of many CuO NWs to orientate at small angle with the surface, being related to the experimental conditions [39]. This feature could be the consequence of weak interactions between the nearest neighbours inside low to medium

density NWs network. As well, processing on a hot plate takes place under a specific distribution of the air flux and in the presence of a vertical thermal gradient which constitutes the differences towards other approaches associated with thermal oxidation. This study does not investigate this matter. The incorporation rate "R_i" of the NWs involves mainly the inclined ones.

The presence of almost vertical NWs being much longer than their appearance in top taken SEM images, with very small projections on surface, add a value "R_ε" to R. In conclusion, the values of apparent R are not representative for C(t) variation. The effective rate that changes the NWs population is given by subtracting both the contribution of the buried CuO NWs and that given by counting vertical CuO NWs with small projection on surface: R_{eff}=R-R_i-R_ε= R[1-(R_i+R_ε)/R]=R(1-γ), where γ = (R_i+R_ε)/R. Therefore we have to express R in term of R_{eff} in (1) as R=R_{eff}/(1-γ) or ΔC(t)/Δt=(ΔC(t)/Δt)$_{eff}$ / (1-γ), resulting expression (2), where the concentration C(t) of the NWs observed on the oxide surface it is determined by their effective generation rate.

$$\frac{1}{C(t)}\left(\frac{\Delta C(t)}{\Delta t}\right)_{eff} = (1-\gamma)\left(ae^{-t/\tau} + b\right) \qquad (2)$$

The single semi-empirical γ parameter of the model, counts for the fraction of those almost vertical NWs and for those incorporated into the oxide layer that correspond to "R_ε" and "R_i" respectively, which cannot be determined by means of this approach that manages a large data collected from the SEM images of 47 samples. The new parameters as α=(1-γ)a and β=(1-γ)b are assumed for simplicity. Expression (2) suggests a differential equation given in (3).

$$\frac{dC}{C} = \left(\alpha e^{-\frac{t}{\tau}} + \beta\right)dt \qquad (3)$$

The concentration of the NWs versus time obtained by integration of equation (3) is:

$$C(t) = C_0 exp\left(\alpha\tau\left(1 - exp\left(-\frac{t}{\tau}\right)\right) + \beta t\right) \qquad (4)$$

The semiempirical parameter γ was estimated at 0.67 to be in the same range with the experimental data regarding CuO-NWs

concentration (4) for samples oxidized 20-40 minutes at 320 ℃ and 340 ℃. A rough estimation of the vertical NWs percentage of 45%, resulted from SEM images collected at different angles, above samples oxidized 40 min at 340 ℃. It means from the expression γ = $(R_i + R_\varepsilon)/R$, that the buried CuO-NWs represent 22% of all and about 40% of those NWs oriented at small angle towards the sample surface. These estimations must be taken with care being linked to restrictive experimental conditions and to the limitations of the assumed model.

The average length of CuO NWs versus time is given in (5), where $\Omega(t) = dl(t)/dt$ represents the growth rate in length of the statistically representative of the NWs that is the derivative of the expression (6). It means to imply pragmatically the average value of $\Omega(t)$ instead of its distribution, that is too difficult. The time variable of the integral (5) represents those NWs that emerged with a delay of ξ seconds relative to the start of the metallic foil oxidation. The integral gives an approximated value of the total length obtained by considering all NWs per unit of surface that emerged and growth during oxidation time "t". $C(\xi)$ and $C(t)$ represent the instant and the final concentration of NWs, respectively.

$$l_{av}(t) = \frac{1}{C(t)} \int_0^t \Omega(t - \xi)\, C(\xi)\, d\xi \qquad (5)$$

Copper oxidation mechanism is controlled by Cu ions diffusion having strong similarities with CuO-NWs growth. Thus, a parabolic low is assumed for the time dependence of the CuO-NWs length given in (6) [40,41].

$$l(t) = p\left(\sqrt{1 + \frac{q}{p}t} - 1\right) \qquad (6)$$

The time dependence of the average length of CuO NWs resulted for oxidation time interval "t" (7) is obtained by using (4) and by introducing the derivate of expression (6) into expression (5):

$$(t) = \frac{1}{C(t)} \int_0^t \frac{p/2}{\sqrt{1 + \frac{q}{p}(t - \xi)}} exp\left(\alpha\tau\left(1 - exp\left(-\frac{\xi}{\tau}\right) + \beta\xi\right)\right) d\xi \qquad (7)$$

This expression was used to fit the corresponding experimental data regarding the average length of CuO-NWs extracted from SEM micrograph as it is shown in Fig. 67. The

optimization was done relative to the parameters p and q. The semi-empirical γ parameter used in the model as 0.67 that was mentioned above, is confirmed by the fitting of data showing in Fig. 67.
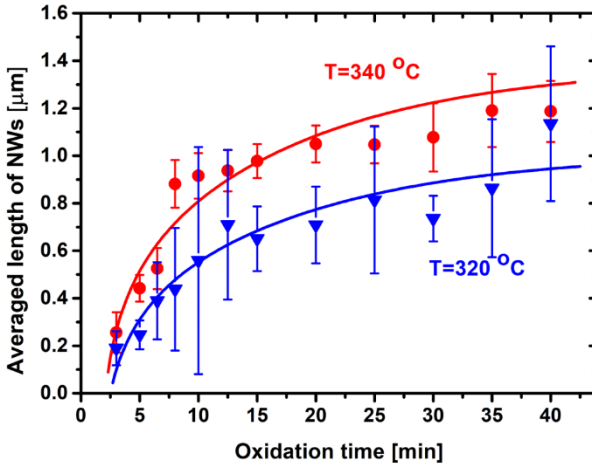
Figure 67. The NWs growth kinetics model expressed by relation (7) and the experimental data of Fig. 7a) corresponding to the average length of the CuO NWs versus time up to 40 minutes of copper oxidation.

Thus, the resulted values of p and q, in respect with the corresponding temperature are: (0.143 μm; 1.21 μm/min) at 340 ℃ and (0.22 μm; 0.51 μm/min) at 320 ℃, respectively.

The satisfactory fitting of the experimental averaged length of CuO NWs versus oxidation time (Fig. 8), gives support for the understanding of early saturation of the kinetic growth, found to be specific close to the threshold temperature. It is explained by the cumulative effects of NWs emerging delays which impedes the initial linear increase of the average length of CuO NWs. Besides, those CuO NWs having small angle orientation towards surface, are easily incorporated inside growing oxide, decreasing the average length of NWs from the expected value as can be observed in Fig. 9a). However, the almost horizontal CuO NWs are broken more probably close to their root by the growth of the oxidation front, which push up along their lengths. Due to Wan-der Waals interaction, the nearest NWs stacked together before being incorporated into the copper oxide, as it is revealed in the SEM micrograph presented in Fig. 9a).
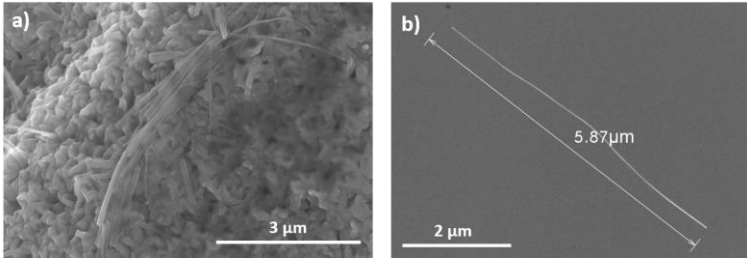
Figure 68. a) CuO NWs of different diameters stacked together before their incorporation inside the growing copper oxide. b) CuO-NW of about 6 microns transferred from oxidized copper foil on SiO2/Si wafer by simple mechanical contact.

An interesting consequence of this study suggests that the increasing population of the CuO NWs with large projections on the surface, should facilitate an easy transfer even for long nanowires of microns range from the copper oxidized foil to another substrate as Si wafer. The simple mechanic contact requesting pressure control produces the fracturing of the almost horizontal nanowires close to their bottom ends, avoiding their multiple breaking [42]. Fig. 68b) shows an example of a single long (6 µm) CuO NW transferred from its native CuO-Cu$_2$O-Cu sample to SiO$_2$/Si substrate as a result of simple mechanical contact between them.

4.7   Single nanowire electric tests

Fig. 69a) shows a CuO NW transferred from its native CuO-Cu$_2$O-Cu sample to SiO$_2$/Si substrate for electric tests. The diameter of the NW is 14.5 nm, whereas the distance between the tungsten contacts is 912 nm (Fig. 69b). The voltage was increased step by step in between -5 V and 5 V. The difference between the work function of CuO NWs at 4.8-5.3 eV and that of tungsten at 4.5 eV indicates the bands bending at metal / p - type semiconductor interfaces. It means that the electron transferred from metal to the semiconductor NW builds a negative space charge specific to a Schottky junction.
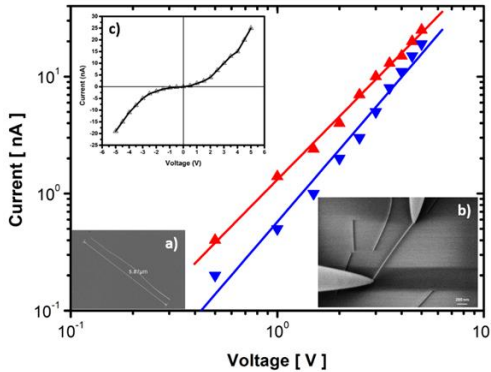
Figure 69. Electric test of a single CuO NW transferred by mechanic contact from its native oxide surface to an oxidized silicon wafer. Log I-Log V plotted data were obtained for both positive and negative polarization of the NW. Insets: a) CuO NW of 5.87 µm in length with a radius of 12 nm after its transfer by mechanic contact from the oxidized copper foil to SiO₂/Si substrate. b) Single CuO NW electrically contacted by pressed tungsten tips using the nano-manipulators placed inside SEM. c) I-V characteristic of a copper NW, the diameter of 14.5 nm and 912 nm in length.

Therefore, the two Schottky diodes model corresponding to both electric contacts, looks adequate for the I-V non-linear characteristic shown in Fig. 10c). The asymmetry of the I-V characteristic is better distinguished using log-log representation for direct and reverse polarization of the NW as it is shown in Fig. 10. The linear dependence of both graphs indicates that the electric charge transport responds to a power low $I \sim V^{\alpha}$. This suggests that space charge limited current (SCLC) it is the main conduction mechanism. The change of polarity keeps the linearity but modifies the slope from 2.05 +/- 0.11 to 1.79 +/- 0.04 nA/V.

Usually the asymmetry of the I-V characteristic is the consequence of the different charge carrier injection through the Schottky diodes at electrical contacts sustained by mechanical pressure. Moreover, the first polarization up to high electric field of 526 KV/cm at 4.8V, usually produces structural changes by the redistribution of Cu ions inside the copper oxide NWs, especially for those with copper excess non-stoichiometry. Under a reversed polarization, applied after a fast voltage removal from 5 V to zero, the I-V curve corresponds to a

different resistance than the previous one. The lowest resistivity obtained at 4 V is 1.8 Ωcm for the first direct polarization.

4.8   Comments and discussion

The CuO NWs behaviour is strongly coupled with structural modifications of the oxide layer during copper annealing. Thus, the pores of the CuO surface oxide layer bypass the incoming Cu ions to meet adsorbed oxygen in the hot spots of fast oxidation, generating NWs rapid growth. The transfer of Cu ions through the oxide layer from the metallic substrate to the surface during the oxidation process makes possible the accumulation of extra copper amount inside the Cu_xO phase with x>2. The competition between the injection of copper at the Cu_xO-Cu interface and its incorporation in continuous growing oxide front located near surface, determines the amount of copper excess relative to Cu_2O stoichiometry. Accurate measurements based on STEM-EDX, XRD and micro-Raman Spectroscopy on the oxidized samples and using the detached oxide sheets have revealed large amounts of copper, strongly exceeding the Cu_2O phase stoichiometry.

Copper aggregation is expected as a result of local accumulation of structural and chemical defects in the metal-rich oxide phase. The Cu ions at the oxidation front could be supplied by local copper reservoirs linked with single or multiple NWs.

Copper precipitates in Cu_2O mono-crystals were reported as a result of thermal treatment above 1000 ℃ [43-46] due to intra-grain activated diffusion. Otherwise, the quasi-reversible electrical properties in Cu_2O have been explained by copper aggregates formation in mono-crystalline Cu_2O [47-51]. The previously published studies show different experimental conditions than those used in this study. Nevertheless, copper clustering in Cu_2O has been reported for copper powder oxidation in air at 350 ℃ [52]. The two possibilities of NWs feeding from the metallic substrate and from local copper clusters, superposes different kinetics. The time dependence of NWs growth considering as the averaged length over the network is influenced by many chemo-physical processes as the built up of local stress [53], electric field developed by static oxide charges [54], amorphous – crystalline local transitions, grains aggregation, all of them influencing the diffusion of Cu ions.

The unexpected quick saturation of the averaged CuO-NWs length versus oxidation time is found close to the threshold temperature 310 - 340 ºC only up to 40 minutes from the start of copper oxidation. The plateau disappears for a longer processing time or above 360 ℃. It suggests that this feature of the NWs growth at the onset temperature is related to the specific structure of the oxide layer considered by us to be related to extra copper content and to its distribution.

4.9   Conclusions

This study focuses on CuO NWs growth, close to the onset temperature of their network at 310 ℃ as a part of a complex air oxidation process of poly-crystalline copper foil on hot plate. Accurate STEM-EDX and XRD analysis measurements on extra copper content in the Cu_2O phase were facilitated by self-detached oxide sheet from the metallic substrate. CuO-Cu_2O stacked phases show extra copper content of 15.2 - 19.1% above the stoichiometry of cuprous oxide in thick samples of 8 microns, obtained by increasing the temperature up to 440 ºC. Part of these atoms belong to Cu nano-crystallites found near the interface with the metallic substrate. The stoichiometric concentration was much more exceeded in samples oxidized up to 60 min, at temperatures ranging between 320 ℃ and 340 ℃. These are metallic-rich oxide layers represented as Cu_xO with $4 < x < 7$ determined on the backside surface of the exfoliated flakes. The embedded copper aggregates generated below the CuO phase become suspicious to play the role of closer Cu ions supplier of the CuO NWs, doing interplay with the metallic substrate on ions migration to the oxide surface. Thus, the NWs growth mechanism at low temperatures has to be related to heavily copper concentration inside oxidic layer, more specific to copper embedded clusters.

The early saturation of the CuO NWs average length versus oxidation time in between 10 and 40 minutes has been observed at 320 - 340 ℃. It was found that two processes contribute to the saturation: the emerging delay of the individual NW relative to the start of the oxidation process and the incorporation into the growing oxide layer of those very inclined CuO NWs.

The quantitative analysis of the above experimental results was done by a semiempirical model. It describes the kinetic growth of the

nanowires length, using the oxidation time dependence of both statistics on CuO NWs population and on their emerging rate. The corresponding data were extracted from SEM micrographs based on the protocol presented above. The model fits the experiment and estimates quantitatively the influence of the emerging delay of the individual NWs, on time dependency of CuO NWs averaged length.

This study contributes to the development of new methods on the controlled growth of CuO semiconductor NWs by thermal oxidation at atmospheric pressure at low density network. The above reported mechanical transfer of the NWs, from the native copper oxide to the silicon wafer, could be considered as a step to self-assembled electrical connections of planar electronic nanotechnology. The applications based on CuO NWs have the advantage of sustainable and eco-friendly preparation methods.

5 Surface Topography of Si/TiO$_2$ Stacked Layers on Silicon Substrate Deposited by KrF Excimer Laser Ablation

5.3 Results and Discussion

Two endeavours generated this contribution: PLD deposition of a buried TiO$_2$ layer as a part of Si/TiO$_2$/c-Si structure, and the application on the AFM data of an adequate approach to reveal the influence of d_{TS} deposition parameter on the topography of the films. The rough surface profile is determined after each consecutive fabrication of TiO$_2$ and Si film. Finally, the sample obtained at d_{TS} that gives the smoothest oxide layer was analyzed by means of XRD, XRR, and ellipsometry.

5.3.1 Deposition of the stacked Si/TiO$_2$ thin films on (100) Si wafer

In order to study the characteristics of the Si/TiO$_2$/n-Si (100) sandwiches structures, the samples were taken out after the TiO$_2$ deposition, and a Ti foil mask was applied to partially cover the surface before the deposition of the top Si layer [9]. Thus, access to both deposited layers was gained for further investigations.

The values of following deposition parameters were considered: substrate temperature 500 ℃, laser pulse energy 500 mJ and the repetition rate of the laser pulse 30 Hz. The surface topography of the

deposited TiO_2 and Si thin films was investigated for several distances between target and substrate as d_{TS}: 4, 5 and 6 cm.

Before the Si deposition we set up the substrate temperature, then we waited for 3 hours for the pressure to reach the lowest value ($P_i \sim 10^{-9}$ Torr), this being in fact the annealing of the preexisting TiO_2 layer in UHV.

In all performed depositions the laser spot was 3 mm^2, substrates rotation was 3 RPM and a deposition time of 600 s for each layer.

5.3.2 AFM characterization of TiO_2 and Si deposited thin films on (100) Si wafer

In this work a special attention was paid to the optimization of the deposited thin films in terms of their surface roughness, which are influencing their optical and electronic properties. The root-mean-square roughness, σ_{RMS} [23], is defined as:

$$\sigma_{RMS} = \sqrt{\sum_{i=1}^{N} \frac{(h_i - \bar{h})^2}{N}} \qquad (1)$$

*w*here: N represents the total number of data points in the analysed profile, hi, represents the value of height for each data point and $\bar{h}$ represents the height mean value over the scanned surface.

The average roughness σ_a represents the arithmetic mean of height deviations from $\bar{h}$:

$$\sigma_a = \frac{1}{N}\sum_{i=1}^{N}\left|h_i - \bar{h}\right| \qquad (2)$$

The Root Mean Square roughness (σ_{RMS}) and the Roughness Average (σ_a) parameters were calculated from the acquired topographic images via an image processing software, using equations (1) and (2) being given in Table 6.

The AFM topography images recorded on annealed Si wafer (S0), TiO_2 and Si thin layers from three different sandwich structures (S1, S2 and S3) corresponding to d_{TS} of 4, 5 and 6 cm are presented in Figure 70 and 71, respectively, all of them revealing a noteworthy uniformity.
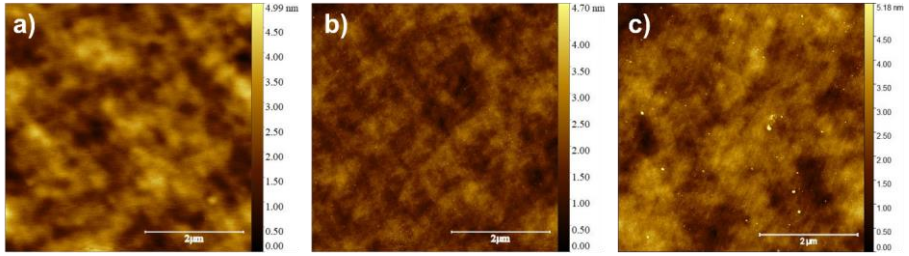
Figure 70. 5x5 µm² 2D AFM topography images of TiO₂ thin films: a) S1; b) S2; c) S3 sample respectively.

The smoothest TiO$_2$ surface is the one deposited at a d$_{TS}$ of 5 cm with a σ$_{RMS}$ = 0.37 nm and σ$_a$ =0.29 nm. The layers deposited at a d$_{TS}$ of 4 cm and 6 cm, revealed higher surface roughness (Table 6). As it can be seen the Si films showed similar behaviour than in the case of oxide films deposition. The smoothest Si surface revealed a σ$_{RMS}$ = 0.36 nm and σ$_a$ = 0.29 nm was obtained for 5 cm d$_{TS}$.
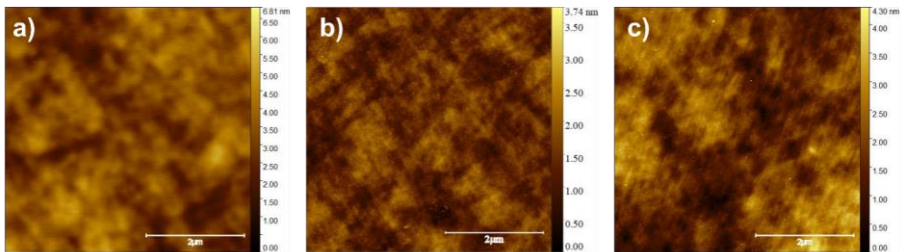
Figure 71. 5x5 µm² 2D AFM topography images of Si thin films: a) S1; b) S2; c) S3 sample respectively.

In Table 6 we show the parameters values associates to samples preparation, highlighting the optimal conditions. For each sample the first line corresponds to the fabrication of the TiO$_2$ layer and the second one to the top Si layer. The values in the table correspond to: index of sample, d$_{TS}$, substrate temperature, laser pulse energy, repetition rate of laser pulses, pressure before ablation, pressure during ablation, calculated σ$_{RMS}$ and σ$_a$ from AFM analysis. As it can be noticed, in all cases, even during ablation, pressure was in UHV interval being lower than 5*10^{-7} Torr.

Table 6. The deposition parameters as: substrate temperature, laser power and pulse frequency, pressure before and during films deposition, and the corresponding σ$_{RMS}$

and σ_a roughness calculated for the 2D topography images recorded for TiO$_2$ and Si thin films (5x5 μm^2).

Sample	DEPOSITION PARAMETERS							AFM ANALYSIS	
	Deposited thin film	d_{TS} (cm)	T (°C)	E (mJ)	RR (Hz)	P_i (Torr)	P_a (Torr)	σ_{RMS} (nm)	σ_a (nm)
S0	Si wafer	x	x	x	x	x	x	0.21 ± 0.026	0.19 ± 0.023
S1	TiO$_2$	4	500	500	30	$6.7{*}10^{-9}$	$4.2{*}10^{-7}$	0.58 ± 0.098	0.46 ± 0.083
	Si	4	500	500	30	$7.6{*}10^{-9}$	$0.9{*}10^{-7}$	0.58 ± 0.077	0.44 ± 0.040
S2	TiO$_2$	5	500	500	30	$5.8{*}10^{-9}$	$4.8{*}10^{-7}$	0.37 ± 0.063	0.29 ± 0.048
	Si	5	500	500	30	$3.9{*}10^{-9}$	$1.0{*}10^{-7}$	0.36 ± 0.024	0.29 ± 0.018
S3	TiO$_2$	6	500	500	30	$6.0{*}10^{-9}$	$4.2{*}10^{-7}$	0.46 ± 0.024	0.35 ± 0.023
	Si	6	500	500	30	$2.2{*}10^{-9}$	$5.0{*}10^{-8}$	0.48 ± 0.090	0.32 ± 0.058

According to all the AFM results, the optimal deposition d_{TS} for both type of materials (TiO$_2$ and Si) is d_{TS} =5 cm (see Table 1, sample S2).

5.3.3 The roughness versus the length-scale related to the target-substrate distance

PSD analysis of the AFM images are the most appropriate procedure on revealing the morphological changes on the surface of thin films according to the deposition conditions. The description of sample roughness using σ_a and σ_{RMS} parameters cannot reveal the modifications of the surface features distribution, associated to their sizes and geometry. Samples characterized by almost the same value of σ_a and σ_{RMS} could show very different rough surface profiles, being the signatures of specific growth mechanisms of the thin films. The PSD function is defined for continuous topography data h(x,y) based on Fourier transform [24] (3):

$$C_{2D}^{PSD}(q_x, q_y) = \lim_{L\to\infty} \frac{1}{L^2} \left| \int_{-\frac{L}{2}}^{\frac{L}{2}} dx \int_{-\frac{L}{2}}^{\frac{L}{2}} h(x,y)e^{-i2\pi(xq_x+yq_y)}dy \right|^2 \qquad (3)$$

where q_x and q_y are the projection on rectangular axes of spatial frequency; L is the maximum value of x and y. The RMS roughness can be calculated using 2D-PSD function (4):

$$\sigma_{RMS}^2 = \iint\limits_{-\infty}^{+\infty} C_{2D}^{PSD}(q_x, q_y)\, dq_x\, dq_y \qquad (4)$$

In the case of isotropic surfaces, the RMS roughness can be expressed by the following relation:

$$\sigma_{RMS}^2 = 2\pi \int\limits_{0}^{+\infty} C_{Iso}^{PSD}(q)\, q dq \qquad (5)$$

where $q = (q_x^2 + q_y^2)^{1/2}$ is the radial spatial frequency [24]. The 1D-PSD function is often used being obtained from 2D isotropic one by imposing to C_{1D} to give the same result in (6) as in (5):

$$\sigma_{RMS}^2 = \int\limits_{0}^{+\infty} C_{1D}^{PSD}(q)\, dq \,; \qquad C_{Iso}^{PSD} = \frac{1}{2\pi q} C_{1D}^{PSD}(q) \qquad (6)$$

The AFM image of the surface is represented by discrete height values $h(x_i, y_j)$, associated to in plane rectangular coordinates given by N_x and N_y, number of steps on x and y axis respectively. The calculation of the 1D-PSD function (4) in the case of discrete data series is based on changing from integration to summation in the frame of fast Fourier transformation algorithm FFT [25].

These investigations focus on the determination of thin films surface morphology as the contribution of both substrate roughness, and the d_{TS} deposition parameter. Therefore, we search for appropriate ways of using PSD on quantitative determination in terms of roughening to be associated with spectral distribution of frequencies [26].
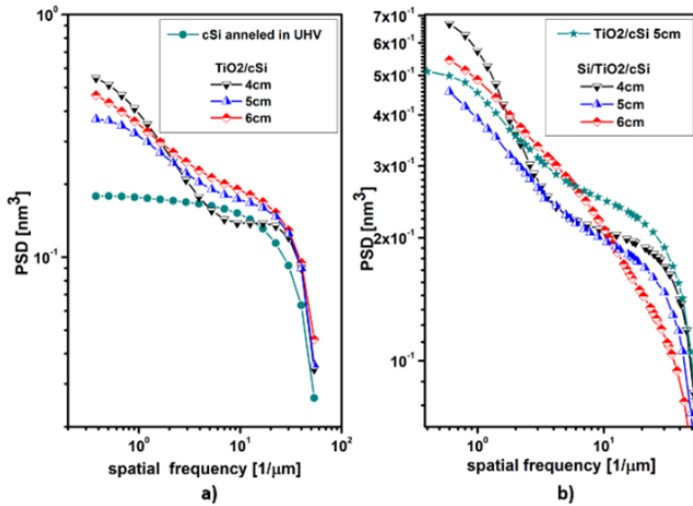
Figure 72. a) The PSD function of TiO₂ thin films deposited on crystalline silicon (c-Si) substrate (green) at different d_{TS} of: 4, 5, and 6 cm. b) The PSD of Si film deposited onto previous TiO₂ layer at the same d_{TS} values. PSD of TiO₂ / c-Si structure considered as substrate for Si layer deposition at d_{TS} = 5cm (green)is given to reveal the changes on surface topography of the prepared samples.

Figure 72 shows the averaged 1D-PSDs of AFM images collected from the surface of TiO₂ and Si films deposited consecutively on (100) Si wafer. The plots correspond to different d_{TS} (4, 5, and 6 cm) inside laser ablation equipment. PSDs diagrams in Figure 4 represent the evolution of surface topography after each deposition from bare crystalline silicon up to the final double stacked layers samples. PSD values calculated from AFM data are given in Figure 4a) in the case of TiO₂ thin films together with the UHV annealed (100) Si substrate in green, being considered as the reference [27].

Figure 72b) gives the PSD data of the same samples, after the Si film deposition onto the previous TiO₂ layer. The PSD of the TiO₂/c-Si structures in green, was included to indicate the feeble changes of surface morphology after Si thin film deposition, in respect with the case of d_{TS} at 5cm. Thus, appropriate data analysis has to amplify these differences searching for quantitative determinations.

The surface topography is given first by the deposited species involved in both smoothing and roughing mechanisms associated with the processing conditions as temperature, pressure, laser

wavelength, pulse time and d_{TS} [20]. Moreover, the contribution of the substrate roughness to the deposited film topography, especially at very small thickness, is revealed by the similarities between the coated and uncovered surface. Therefore, the estimation of the direct influences of the d_{TS} on the rough surface profile requires the extraction of the substrate imprinting features into the deposited thin film that could propagate from the interface up to the top of the sample. It means, to determine the changes of the roughness associated to spatial frequency range, determined by the coverage produced by the incoming particles relative to the initial topography. PSD associated to TiO_2 and Si films in Figure 4 have been used in the frame of mathematical expression that link the roughness to the spatial frequency or wavelength. We have considered the roughness versus length scale (RLS) function $\sigma(\lambda; \lambda_{min})$, defined in (7) [24,28].

$$\sigma^2(\lambda; \lambda_{min}) = \int_{1/\lambda}^{1/\lambda_{min}} C_{1D}^{PSD}(q)\, dq \qquad (7)$$

where $\lambda min = 1/q_{max}$, it is the parameter associated to the length-scale $\Delta\lambda = \lambda - \lambda_{min}$, with λ representing the spatial wavelength. λmin has an imposed value of 10 nm, being required to reject the artifacts associated to the radius of the AFM tip used in this study. $\sigma(\lambda; \lambda_{min})$ has spectral significance being a function that can be defined versus spatial wavelength or spatial frequency. The graphical representations for all data calculated by relation (5) were plotted below using λ on abscissa instead of the length-scale $\Delta\lambda = \lambda - \lambda_{min}$ that involve a fixed shift of 10 nm. Moreover, the above RLS function is used to express in percentages the variation of the roughness produced by the deposition of the TiO_2 layer relative to that of the c-Si substrate [29].

$$\varepsilon_{TiO_2}(\lambda) = \frac{\sigma_{TiO_2}(\lambda) - \sigma_{c-Si}(\lambda)}{\sigma_{c-Si}(\lambda)} * 100\% \qquad (8)$$

Figure 73a) reveals the values of the RLS function on TiO_2 thin film, calculated for several values of d_{TS}. The changes of surface roughing by the oxide layer deposition, relative to the initial topography of the (100) Si substrate are shown in Figure 73b)

according to the relation (6). Titanium dioxide roughness is higher than that of Si wafer for all values of d_{TS} parameter: 4, 5, and 6 cm. These quantitative determinations indicate that for the length-scale associated to 20 nm < λ < 550 nm the smallest roughness is obtained at d_{TS}=4cm being almost the same as for Si substrate in between 70 nm and 200nm. The spatial wavelength λ of the surface features below 550 nm indicates that the local roughing is increasing systematically as the substrate is placed far away from the ablation source as d_{TS} is modified from 4 to 6 cm. This effect corresponds to the diminishing of the incident particles number with orientations at large angles relative to the normal direction towards the substrate. Under these conditions the shadowing process it is expected to contribute on the increasing of roughness [30]. The wide angle distribution of the incoming particles at the smallest d_{TS} distance leads to the conformity of the rough surface profile on top of the deposited TiO_2 layer with that of the (100) Si substrate in between 70-250 nm.
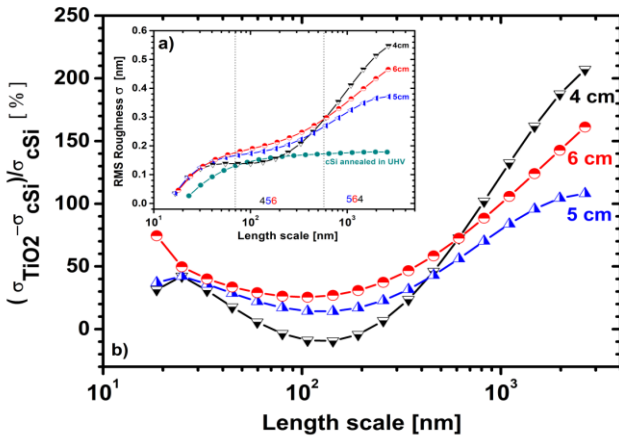
Figure 73. a) TiO_2 thin film roughness calculated using radial PSD versus the length scale corresponding to d_{TS} of 4, 5, and 6 cm. The c-Si substrate roughness is represented in dark green. b) TiO_2 thin film roughness variation relative to (100) Si substrate for the same d_{TS} values, versus the length scale.

It is interesting that the smallest values of RLS obtained at 70 – 550 nm for samples deposited at d_{TS} = 4 cm become greater than the other ones above < 600 nm. The contribution of the large features to the overall roughness changes the top of the smoothness above 600 nm in Figure 5a) and 5b). Thus, the best TiO_2 sample was

obtained at d_{TS}=5cm, by considering entire length scale of spatial wavelength into expression (7).

$$\varepsilon_{Si}(\lambda) = \frac{\sigma_{Si}(\lambda) - \sigma_{TiO_2}(\lambda)}{\sigma_{TiO_2}(\lambda)}$$
$$* \ 100\,\% \tag{9}$$

Figure 74 shows the same type of data as those in Figure 73 but for silicon thin film deposited above the previous TiO$_2$ layer. Thus, Figure 74a) gives the values of the RLS function associated to Si thin film, calculated for several values of d_{TS}. In this case, the variation of the rough surface profile from that of TiO$_2$ to the on top Si layer $\varepsilon_{Si}(\lambda)$ is considered relative to that of titanium dioxide film, being this time like a new substrate (9).
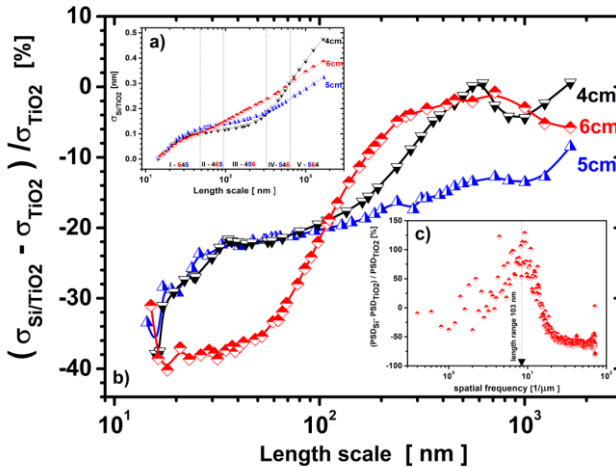
Figure 74. a) Si thin film RMS roughness versus the length scale at different values of d_{TS} b) The relative roughness variation between Si and TiO$_2$ thin film surfaces, the last being the substrate coverage of the second layer deposition. The highest slope found in the case of the sample prepared at d_{TS} = 6cm, close to the crossing point, corresponds to surface features distribution peak at 8.5 µm-1 shown in inset c) that gives the relative variation of PSD amplitude of silicon layer relative to TiO$_2$ thin film acting as substrate coverage.

The negative values on the vertical axe in Figure 74b) of all samples, indicate that silicon deposition on TiO$_2$ produces surface flattening along the full scale of the spatial wavelength.

The expected processes that lead to smoothing is surface migration of silicon atoms by reemission and diffusion, influenced by the oxide coverage. The smoothest samples corresponding to the spatial wavelength between 20 nm and 117 nm was obtained at d_{TS} of 6 cm. Contrary, above the crossing point at 117 nm the same sample turn to the highest roughness of all. Around this value the slope reaches the highest value. It is associated to surface features belonging to size distribution centred close to 8.5 μm^{-1} as it is revealed by inset of Figure 6c). Here the difference between PSD Si and PSD TiO_2 given in Figure 4, divided to PSD TiO_2 is plotted versus spatial frequency [26]. The peak corresponds to the length scale of 103 nm being close to the crossing point in Figure 74b).

The silicon films deposited at d_{TS} of 4 and 5cm have similar dependence versus the length scale up to the crossing point. The smoothest silicon film was obtained at d_{TS} = 5 cm according with the roughness corresponding to entire length scale of spatial wavelength. The above data of the rough surface profile of TiO_2 and Si films remain unexplained at the length scale greater than 500 and 100 nm respectively. Anyway, the interpretation lies on finding the dominant process of the front roughness formation during PLD deposition regarding: shadowing, reemission, and surface diffusion [30], by similar investigations.

5.4 Structural and optical characterization of TiO_2 thin films

One goal of this contribution is to build TiO_2 layer buried in silicon by PLD consecutive depositions of the oxide and Si films on (100) Si wafer with thickness in the range of tens of nanometer. The improving of the roughness is critical for both interfaces of the buried TiO_2 layer in respect with electrical and elastic properties requested for applications in the field of sensors or electronic devices. Complementary techniques as XRD, XRR, and spectrometric ellipsometry were used for the characterization of the smoothest TiO_2 layer obtained by laser ablation deposition, according with the optimization of the d_{TS} parameter.

5.4.1 X-ray diffraction and X-ray reflectivity

The naturally occurred phases of TiO_2 are anatase, rutile and brookite [31-34]. The last one is of high importance especially as photocatalysts, due to either oxidative and reductive manifestation of

the exposed surface associated to (201) or (210) respectively. Brookite thin films of good quality are much more difficult to be obtained being in a mixture with anatase or rutile [31,35,36]. The XRD diffraction pattern of the TiO_2 film in Figure 75c) is dominated by (100) Si substrate at 2Θ 69.15° [37,38]. The following peaks were associated to brookite phase in the diffractogram presented in Figure 75a): 31.37° (121), 44.93° (122), 63.3° (321), 82.02° (063) with magnification for the last two reflections shown in Figure 75b) [31,36,39]. The intense peaks observed at 31.370 and that at 44.93° were reported in reference [31] being associated to brookite phase of PLD deposited films on Si (111) at 750 °C. Furthermore, in [40] are given similar results for ALD (atomic layer deposition) on the same substrate. Brookite-rich thin films of 95% were obtained by PLD after annealing at 290 °C [41]. The above-mentioned reports together with the partial XRD signature shown in Figure 75a) and 75b) suggests the formation of the brookite phase into the deposited TiO_2 layer. Moreover, the expected peaks of anatase or rutile phase were not identified as other studies reported in the case of deposited TiO_2 thin films [16, 34]. Unfortunately, the resulted conclusion about the formation of a rich-brookite oxide [39] must be taken with care due to the very thin TiO_2 oxide layer combined with the missing of some expected XRD peaks.
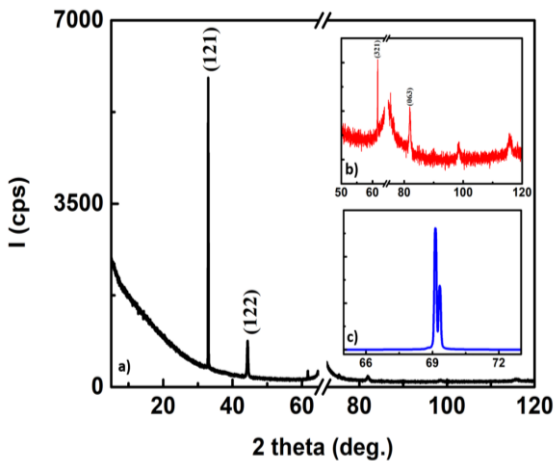

Figure 75. a) XRD Diffractogram of TiO_2 layer (sample S2) in the range 5 – 120 deg. showing the specific peaks of brookite, b) zoom in, c) the peak of the Si (100) substrate.

X-Ray Reflectivity (XRR) was used in order to examine the roughness and the thickness of the TiO$_2$ layer. The roughness determined in the XRR measurement shown in Figure 76a) for the TiO$_2$ layer obtained in optimal conditions (sample S2) is 0.37 nm, being in agreement with the AFM data for the same layer (Table 6) [42].

The variation of the X-Ray reflectivity shown in Figure 76a) is related to the thickness of TiO$_2$ film [43]. The reflectivity oscillation profile (r) is described by the following expression:

$$\cos\left(\frac{4\pi d}{\lambda x\sqrt{sin^2\ \theta-2\delta}}\right) \hspace{4cm} (10)$$

where d is the thickness, λ_x is the wavelength, θ is the incident angle and δ is the refractive index of X-Ray.
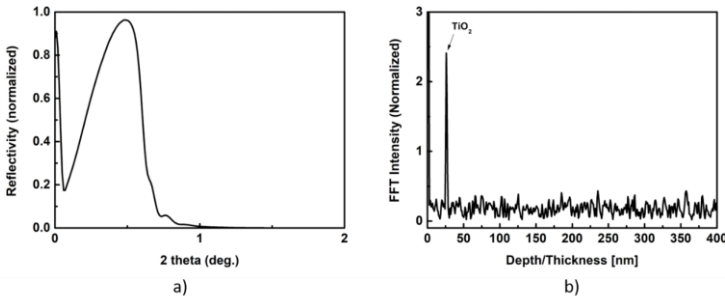
Figure 76. a) X-Ray reflectivity curve of TiO$_2$ on n-Si (100) b) The Fourier transform profile of the reflectivity curve.

The thickness of the layer is given by the peak position in the profile of Fourier transformation with the horizontal axis set as $\sqrt{sin^2\ \theta-2\delta}$. The thickness of the TiO$_2$ layer was found to be 27 nm as it can be seen in Figure 76b).

5.4.2 Ellipsometry

Optical parameters and the thickness of the thin oxide layer were determined by means of spectroscopic ellipsometry, in order to corroborate with XRR results. The optimal fitting within the Cauchy model of the Ψ and Δ parameters, as it can be seen in Figure 77a), has found the TiO$_2$ layer thickness to be 26.5 nm which is in good

agreement with XRR measurement mentioned above. It could be adequate to mention that the variation of thickness relative to the averaged TiO_2 and Si thin films thickness are lower than 7.2% and 10.1% respectively.

The refractive index namely its real and imaginary parts: n, k respectively that result from the fitting procedure are given in Figure 77b) versus the light wavelength. The high value of n and its dependence on the wavelength in Figure 77b) is comparable to those reported about rich- brookite TiO_2 films [40].
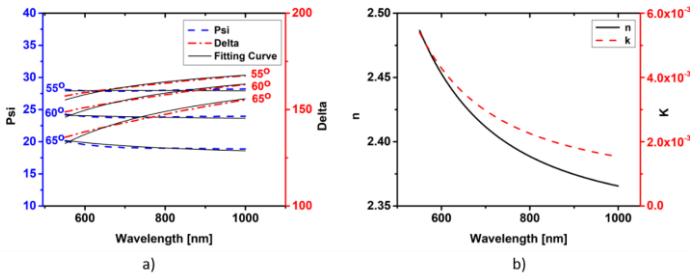

Figure 77. a) Fitting of ellipsometry results Ψ and Δ for 3 measuring angles, b) optical constants for TiO₂ layer used for fitting

5.5   CONCLUSIONS

This work investigates the profile of the rough surfaces for both TiO_2 and Si thin films deposited by PLD on silicon wafer. On top silicon film and the buried oxide layer, enclosed in Si/TiO$_2$/c- Si structures, were prepared for several target-substrate distances d_{TS}, ranging between 4 and 6 cm. We focused on the surface topography in relation with the deposition parameter d_{TS}, and with the initial substrate morphology, considering that at small thickness of the deposited layers their physical properties are more influenced by roughness. The change of d_{TS} value is associated to the modification of angular distribution of the incoming particles on substrate. Therefore, the RLS function associated to PSD-AFM analysis, has been proposed for its sensitivity that gives responses to the evolution of surface topography from bare (100) Si wafer up to on top deposited layer of the Si/TiO$_2$/cSi stacked structure. Thus, the spectral characteristic of the RLS function has the advantage of showing the changes of the roughness versus the length-scale after each deposition, highlighting the influences of the d_{TS} parameter. Furthermore, the topography of the deposited layer

results as a combination of the initial roughness of the substrate and the deposition parameter d_{TS}. Relative RLS function takes into account both influences. Thus, we show that the TiO_2 deposition on Si (100) produced an increase of the roughness in the range of those features having spatial wavelength greater than 100 nm (Figure 5b). Contrary the Si deposition onto TiO_2 determine the smoothing of the initial oxide surface (Figure 6). Thus, the mechanisms of thin films growth can be revealed by adequate AFM data analysis, paving the way to useful physical models that correlate deposition parameters to the features built by particle assembling on surfaces.

In conclusion we show that relative RLS based on PSD function, used for AFM data analysis, reveals quantitatively the evolution of surface profile on top layer of the $Si/TiO_2/(100)$ Si stacked films after their consecutive depositions, in relation with both substrate and with the d_{TS} distance.

6   Towards Uniform Electrochemical Porosification of Bulk HVPE-Grown GaN

6.3   Experimental Results and Discussion

The anodic etching of the N-face of the wafer in HNO3 electrolyte starts with the formation of a porous layer with the thickness around 2 µm with most of pores propagating perpendicularly to the wafer surface. Underneath this layer, one can distinguish a complex structure consisting of porous pyramids with dimensions in the range of tens of microns (Fig. 78). These structures disclose the inhomogeneity of electrical conductivity of the wafer near the N-face.
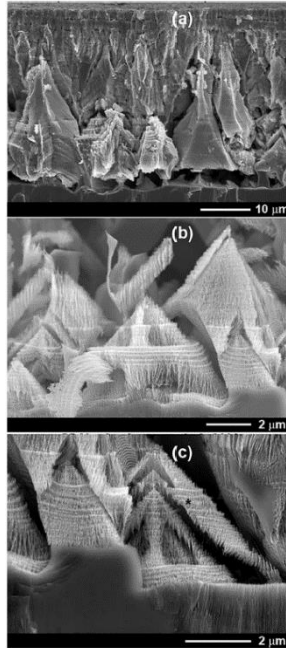
*Figure 78. SEM micrographs of porous GaN morphologies produced in depth from
the N-face by EC etching in 0.3M HNO3 electrolyte under 15 V anodic bias: (a)
general view of the produced porous layer, and magnified view of pyramids (b, c).*

A model has been previously proposed to explain the
formation of these three-dimensional self-organized architectures
during overgrowth of V-type pits occurring in conditions of variable
growth direction [50]. According to this mechanism, the HVPE growth
results in the formation of pyramids consisting of layers with
alternating high and lowconductivity. The complex structure of each
of these pyramids is illustrated in cross-sections (b) and (c) of Fig. 78.
One can see the spatial modulation of porosity in pyramids caused by
spatial modulation of electrical conductivity. The cross-section of the
pyramid marked with asterix in Fig. 78c reveals highly porous layer
separated by totally etched layers in the direction parallel to the
pyramid surface. The etched layers were of high conductivity, and
they were totally etched due to the higher etch rate in high conductivity
material.

Different patterns of inhomogeneous electrical parameters in
the HVPE grown GaN near the N-face revealed by EC etching are
illustrated in Fig. 79. One can observe non-etched regions with low

conductivity nearby layered structures (right image), arrays of nanowires formed in regions with high conductivity (left image), and more homogeneous porous regions with pores propagating perpendicularly to the wafer surface (bottom image). The diameter of pores and the pore wall thickness is in the range of 15–25 nm in these regions. This is indicative of the fact that the wafer becomes more homogeneous with increasing the depth from the N-face.

Usually, two types of pores can be generated in semiconductor compounds: current line oriented (CLO) and crystallographically oriented (CO) pores. [51]. The characteristics of the pores (shape, velocity of growth, etc.) depend on the specific anodization conditions. It was established that CO pores grow at current densities lower than a certain threshold value, whereas CLO pores grow at current densities higher than the threshold value. The threshold values depend strongly on the free carrier density in semiconductor crystal, electrolyte concentration, and temperature. The main feature of the CO pores is that they grow along definite crystallographic directions.
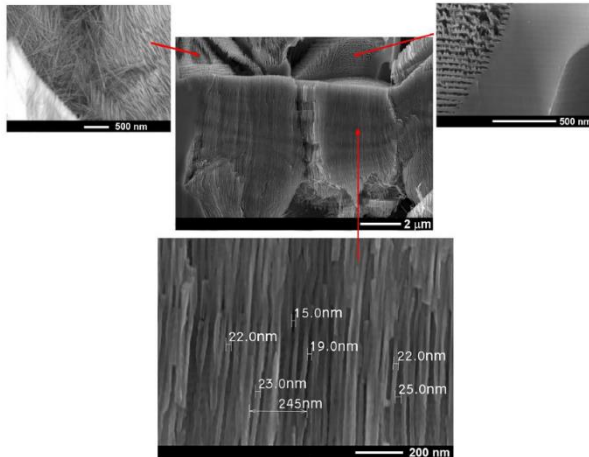
Figure 79. Various nanoporous morphologies obtained at a depth of 40 µm from the N-face upon etching in 0.3M HNO3 electrolyte.

The influence of the applied anodization voltage on the porosification process is shown in Fig. 3, which presents morphologies obtained with anodization in HNO3 electrolyte near the N-face. One can see the formation of lamellar pyramidal structures upon anodization at 18 V (Figs. 80a, 80b) and structures with much

smaller degree of porosity obtained under anodization at 10 V, which prove to be more robust and are not destroyed upon sectioning (Fig. 80c), as well as structures containing both CLO and CO pores (Fig. 3d) produced under anodization at 5 V. The formation of crystallographically oriented pores is indicated by their triangular shape in the mid part of Fig. 80d and in the inset. Recently, the influence of the applied anodization voltage upon the shape of pores obtained by lateral anodic etching of MOCVD grown GaN in HNO3 and NaCl [52,53] electrolytes was investigated. It was shown that the cross-sectional shape of pores can be modified from triangular pores to quasi-circular pores with increasing the voltage, which is indicative of the possibility to tailor the shape of pores by design.

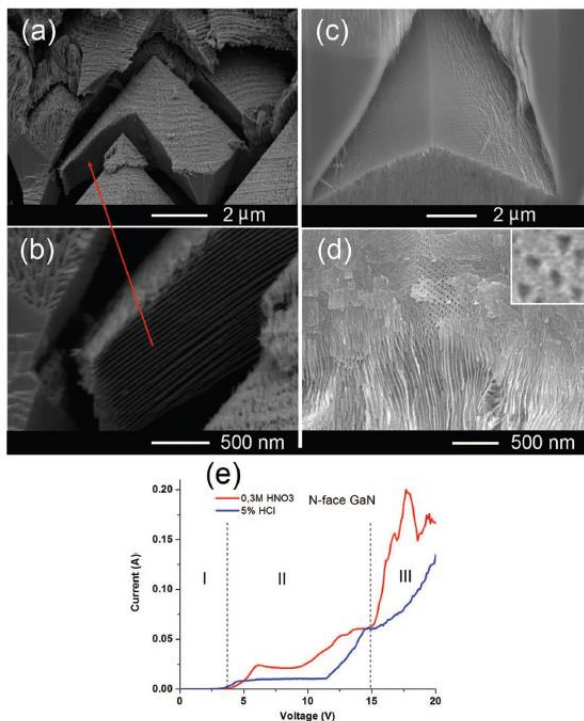*Figure 80. SEM micrographs of porous GaN morphologies produced in depth from the N-surface by EC etching in 0.3M HNO3 electrolyte under 18 V (a,b), 10 V (c) and 5 V (d) anodic bias. The polarization curves measured at the beginning of the anodization process of GaN on the N-face are shown in (e).*

Note that the CO pores were observed in other three III-V semiconductors: n-InP, n-GaP and n-GaAs [51,54]. The main

directions of growth for the CO pores in the compounds involved are <111>B directions. Another important characteristic of the CO pores is their tendency to self-organized branching along the four <111>B directions. It is important to note that the branches can intersect each other [55].

The electrochemical dissolution behaviors of the N-face GaN in HNO3 and HCl solutions are characterized by the I–V curves shown in Fig. 80e. Three regions with different slopes can be distinguished in the polarization curves. A very low current level was registered in region I when the applied potential was lower than the breakdown potential or pore formation potential (PFP) equaling 3.5 V. As the potential is increased above 3.5 V, the anodic current first slowly increases, and above about 10 V the current rises steeply. The region II was attributed to the pore formation with low degree of porosity. Further increase in applied voltage (more than 15 V) leads to the formation of pyramidal structures with higher porosity which can be easily destroyed with simultaneous formation of nanowires and nanowalls (region III). At higher applied biases (more than 20 V) isotropic electrochemical polishing occurs.

The observation that the wafer becomes more homogeneous with increasing the depth from the N-face is corroborated by the analysis of porous morphologies formed nearby the Ga-face of the wafer. The EC etching in HNO3 electrolyte on the Ga-face of the wafer starts at some nucleation points determined by surface defects and imperfections and proceeds in radial directions at the initial phase of the EC process (see Fig. 81), similar to the process of pore development disclosed previously in GaP [56]. Usually, the density of the nucleation points (etch pits) depends on the doping concentration of the sample and the applied anodization voltage. The lower is the doping level, the higher is the applied voltage needed for the formation of nucleation points. On the other hand, the higher is the applied voltage at a given doping level of the wafer, the higher is the density of the generated nucleation points. Note that, at a high enough applied voltage, the density of nucleation pointswill correlate with the density of threading dislocation emerging at the surface of the wafer.
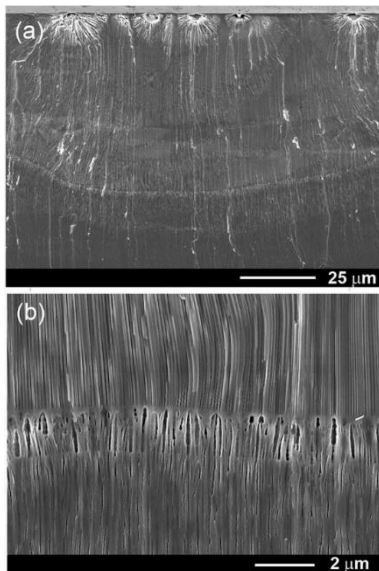
Figure 81. (a) Cross-section SEM micrographs of a porous GaN structure produced in depth from the Ga-face by EC etching in 0.3M HNO3 electrolyte under 100 V anodic bias. (b) Multilayer porous structure obtained by increasing the applied voltage to 140 V for a short period of time (25 sec) during the EC etching.

Later-on, the pore growth is dominated by a self-organized process which results in the formation of pores in the direction perpendicular to the wafer surface. The morphology of pores is much more homogeneous as compared to that formed nearby the N-face, which is indicative of a more homogenous electrical conductivity. Porous matrices with pores perpendicular to the wafer surface can be produced at depths larger than 50 μm, as illustrated in Fig. 81a. Apart from that, porous structures with spatially modulated degree of porosity can be obtained by changing the anodization voltage during the pore growth process, see Fig. 81b. It is to be mentioned, however, that the anodization voltage should be increased up to values as high as 100 V to perform porosification nearby the Ga-surface of the wafer. This means that the conductivity of the wafer is much smaller near the Ga-surface as compared to that inherent to the N-face. Taking into account the processing phase diagram for EC etching given in Refs. [25,34,57], one can estimate that the doping concentration is around 10^{19} cm^{-3} near the N-face, and about one order of magnitude smaller near the Ga-face. However, these values are only a rough estimate. Note that the Hall effect measurements would provide

information about the integral doping concentration of the free charge carriers over the depth of the wafer.

Figure 82a demonstrates a quite uniform distribution of pores on the surface after removing the nucleation layer, while Fig. 82b shows the pore image in cross-section. Since the depth of pore penetration is high enough, the nucleation layer was removed by a simple cleavage. Mechanical removal was used to avoid the impact of electrolytes during the wet isotropic etching upon the estimation of the diameter of pores and wall thickness.

The diameter of pores and width of the walls is around 60–70 nm. It is to be noted, however, that according to our systematic SEM investigations the ratio of the pore diameter to wall thickness increases with the increase of the anodization voltage. Particularly, the diameter of pores reaches 130 nm when the anodization voltage equals 150 V.

Figure 82. (a) Frontal SEM micrograph of pores produced at the Ga-face by EC etching in 0.3M HNO3 electrolyte under 100 V anodic bias after removal of the nucleation layer. (b) Cross-sectional SEM micrograph taken after sample porosification.

It is believed that highly corrosive, acidic or alkaline etchant such as: HF, HNO_3, H_2SO_4 and KOH are indispensable for etching chemically stable GaN. Note that these conventional etchants have many disadvantages, first of all because they are unsafe and

environmentally unfriendly. Therefore, one of major challenges for etching GaN is to search environmentally friendly electrolytes. Schwab et al. recently reported neutral electrolytes such as NaNO3 and NaCl for etching GaN [58]. Photoelectrochemical etching of GaN in environmentally friendly ionic liquid electrolytes has been also proposed to address this issue [59-61].

We found that HVPE-grown GaN can be efficiently porosified in NaCl electrolyte. Fig. 83a shows a SEM micrograph of the N-surface
of the GaN wafer after etching in a 3.5M NaCl electrolyte under 15 V anodic bias. A clear formation of porous circular/hexagonal rings is observed at the surface. Such morphologies with alternation of regions with high and low degrees of porosity are typical for the N-surfaces subjected to EC or photoelectrochemical etching [50], and they were attributed to the spatial modulation of the electrical conductivity in the HVPE-grown GaN samples, according to the previously proposed model of HVPE growth. There porous structures develop from the surface to the bulk, as illustrated by a cross-sectional image in Fig. 83b, and the pores penetrate rather deep in the wafer, similarly to the case of etching in the HNO3 electrolyte, resulting in the generation of pores oriented perpendicularly to the wafer surface in deeper regions exhibiting a more uniform conductivity (Fig. 83c).
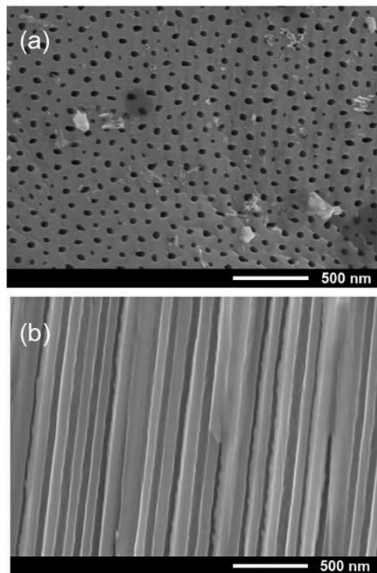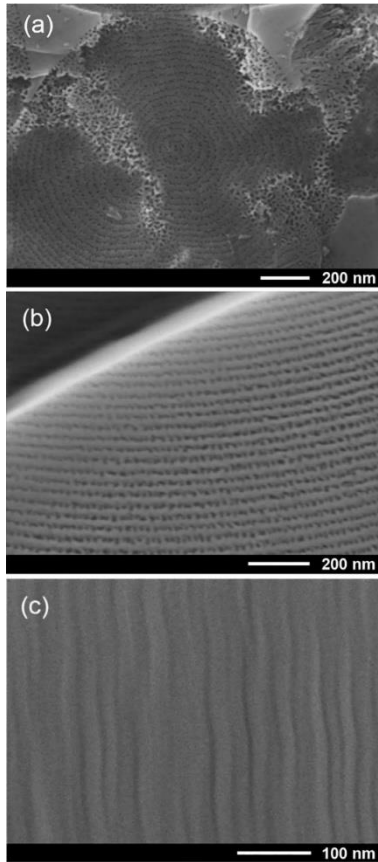
Figure 83. (a) Frontal SEM micrograph of pores produced at the N-face by EC etching in 3.5M NaCl electrolyte under 15 V anodic bias. (b) Cross-sectional view near the N-face. (c) Cross-sectional SEM micrograph of pores in depth from the N-face.

Similar results are obtained with EC etching of GaN wafers in an HCl-based electrolyte, as illustrated by SEM images taken in crosssection in regions situated far enough from the N-face, i. e. in regions with a relatively uniform spatial distribution of the conductivity (Fig. 84). One can see from Fig. 84b the formation of pores with transverse dimensions of 5–10 nm, similar to those produced under EC etching in the NaCl-based electrolyte (Fig. 83c). The similarities in EC etching of GaN in HCl-based and NaCl-based electrolytes may support the suggestion put forward by Zhang et al. concerning the existence of an alternative mechanism of EC etching of GaN[59], in addition to the broadly accepted etching mechanism based on

semiconductor material oxidation in the EC etching process with subsequent dissolution of the oxide and formation of pores. In case of photo-assisted EC etching of gallium nitride, the predominant intermediate product of the etching process is commonly accepted to be Ga_2O_3 oxide due to the increase of Ga-O bonds on the etched GaN surface [62]. However, Ga_2O_3 should not be soluble in electrolytes with neutral pH, which is indicative of the existence of another etching reaction for neutral etchants. Taking into account the similarities of etching in HCl and NaCl electrolytes, one may suggest that Cl− plays a major role in the etching process.
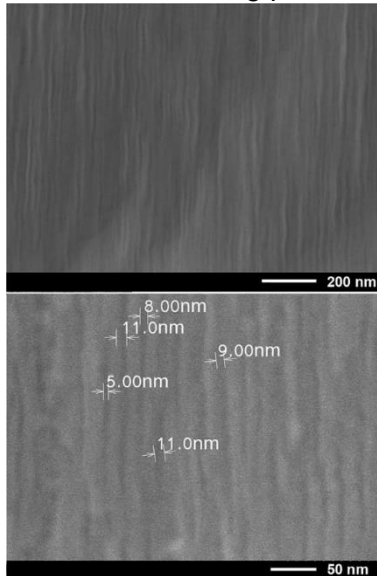
Figure 84. Cross-sectional SEM micrographs of pores produced in depth from the N-face by EC etching in 5% HCl electrolyte under 15 V anodic bias.

The reactions for the formation of porous GaN inHNO3 electrolyte can be described by Eq. 1 and Eq. 2 representing electrochemical and chemical reactions respectively [63]. After the n-GaN crystal is immersed in the electrolyte, an equilibrium of Fermi levels of both materials results in bending of semiconductor band edges at the junction. The band bending involves the movement of charge carriers from one side of the Schottky junction to another and vice versa. When the potential is applied, and etching voltage is higher than the flatband potential, the electrons will rapidly deplete at the interface and the space charge region (SCR) will form. The

generated holes at the GaN/electrolyte interface will participate in the oxidation of the GaN crystal:

$$GaN + 3H_2O + 3h^+ \rightarrow Ga(OH)_3 + 1/2N_2 + 3H^+ \quad [1]$$

Due to the fact that the oxidized product of the GaN is not thermodynamically stable in the acid medium, it will dissolve into Ga3+ for further etching of GaN:

$$Ga(OH)_3 + 3H^+ \rightarrow Ga^{3+} + 3H_2O \quad [2]$$
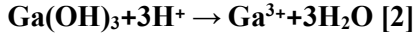
Let pass to the discussion of the results of STEM analysis of nanostructures resulting from EC etching of HVPE-grown GaN. Figure 85 shows the STEM images taken in regions similar to those shown in Fig. 79 left, which exhibit arrays of nanowires and fragments of nanowalls. The images were registered using different detectors, namely, secondary electrons (SE) – left, atomic mass contrast (ZC) – middle, and transmission electrons (TE) – right, at the same location on the sample at different magnifications: x100K – first row, x300K – second row, and x700K – third row.

Figure 85. STEM micrographs of GaN nanostructures resulting from EC etching. Different detectors were used: secondary electrons (SE) – left, atomic mass contrast (ZC) – middle, and transmission electrons (TE) – right, at the same location on the sample at different magnifications: x100K – first row, x300K – second row, and x700K – third row.
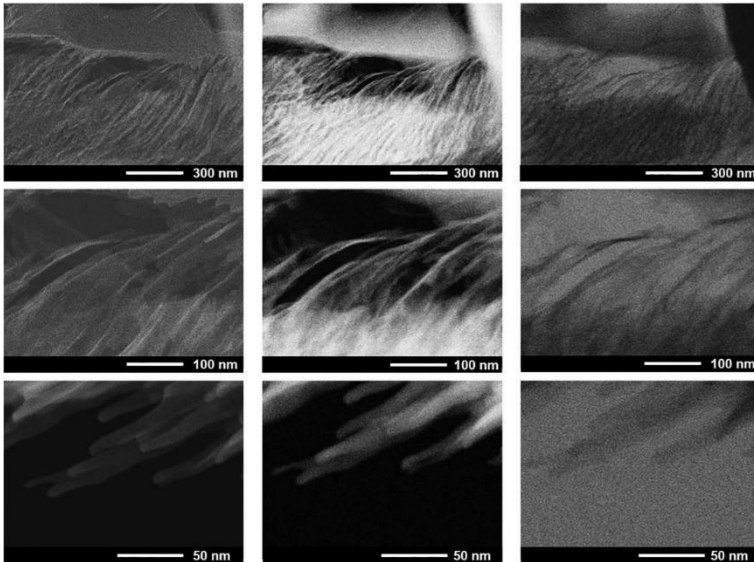
The HR-STEM image acquired in area of the last row in Fig. 85 is shown in Fig. 86. Two lattice spacings between adjacent planes

along reciprocal perpendicular directions were found to be of 0.2818 nm and 0.2585 nm. These values correspond to spacing between adjacent (1-100) and (0001) planes of thewurtzite GaN lattice, respectively [64,65]. The value of 0.2818 nm is larger than the interplanar spacing of stressfree GaN along the [1-100] direction (0.276 nm). It means that the GaN nanowire lattice is strained in this direction, and the estimated strain value is around 2%. Note that a similar strain value along this crystallographic direction was found in porous GaN structures produced by EC etching in a NaNO3 solution [66].

An important observation from Figs. 86d, 86e is that the angle between the [1000] and [1-100] directions differs by 2° from 90°.
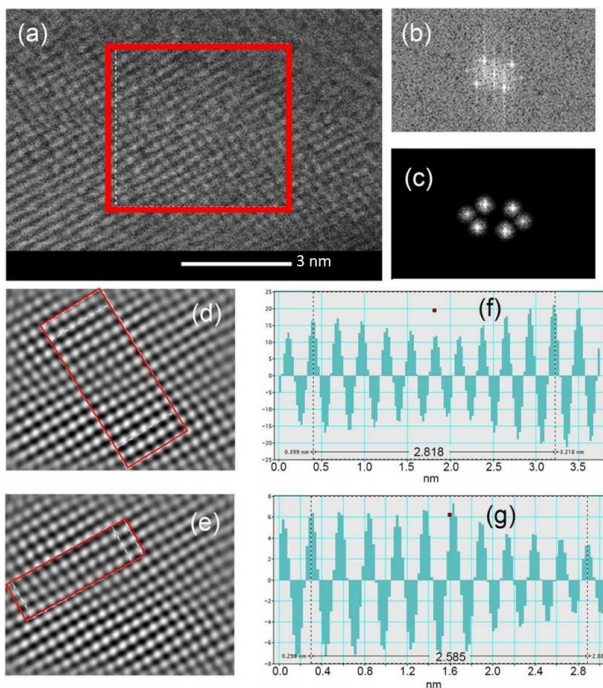
Figure 86. HR-STEM analysis of a GaN nanowire produced with EC etching. (a) Area chosen to perform d-spacing measurements. (b) FFT filtered image from selected area. (c) Applied mask on the FFT filtered image from the selected area. (d, e) Inverse FFT images extracted from the FFT filtered image in the selected area. (f, g) Profiles obtained from the marked area in the inverse FFT image.

Nevertheless, the investigations demonstrate that the grown GaN wafer is single crystalline as a whole. Therefore, the revealed by

EC etching inhomogeneities are related to spatial modulation of the electrical conductivity of the material rather than to crystal structure inhomogeneity. This is an encouraging finding which is indicative of the prospects of producing homogeneous porous structures over the entire HVPE-grown wafer, providing that the issues of reducing the modulation of doping during the crystal growth are properly addressed, particularly by avoiding the formation of V-type pits in the growth process. The feasibility of uniform porosification of bulk GaN is demonstrated by the production of deep enough homogeneous porosity near the Ga-face of the HVPE-grown wafer.

6.4   CONCLUSIONS

The results of this study disclose different porous morphologies produced by EC etching in the depth of a HVPE-grown wafer with respect to the N- or Ga-face.

Complex porous pyramidal-type structures are formed at a depth of several tens of micrometers from the N-face, while homogenous porous matrices with pores oriented perpendicular to the wafer surface are generated at a depth of up to 50 µm at the Ga-face. These features are explained by variations in the electrical conductivity across the wafer resulting from the mechanisms of the HVPE growth.

Possibilities of producing porous structures in environmentally friendly electrolytes of the NaCl-type are demonstrated.

The comparison of porous morphologies with those obtained under anodization in HCl electrolytes suggests the existence of an alternative mechanism of EC GaN etching, in addition to the broadly accepted etching mechanism involving the formation of a Ga2O3 oxide as an intermediate product of the EC etching.

The HR-STEM analysis of the produced GaN porous structure demonstrates the preservation of the good wurtzite-type crystalline phase of the material.

The obtained results pave the way for wafer-scale nanoporous GaN production for various optical, optoelectronic and photonic applications.

EXPERIMENTAL TEHNIQUES SKILLS LEARNED DURING PhD STUDIES

1. SEM+EDX+EBL+ nanomanipulators;
2. TEM+SEM+ZC+EDX;
3. SEM+FIB+EDX;
4. PLD;
5. CNT;
6. CRYO;
7. UV-VIS;
8. MS;
9. Ellipsometry;
10. MANTIS Thin Films deposition;
11. TGA;
12. Excimer Laser KrF;
13. Spin coater;

PUBLICATIONS LIST

ISI paper:

During PhD:
1) C. C. Moise, A. Pantazi, G.V. Mihai, A. Jderu, M. Bercu, A.A. Messina, M. Enăchescu, Surface Topography of Si/TiO2 Stacked Layers on Silicon Substrate Deposited by KrF Excimer Laser Ablation, Coatings 11, (2021), 1350. https://doi.org/10.3390/coatings11111350
2) C. C. Moise, L.B. Enache, V. Anăstăsoaie, O. A. Lazăr, G. V. Mihai, M. Bercu, M. Enăchescu, On the growth of copper oxide nanowires by thermal oxidation near the threshold temperature at atmospheric pressure, Journal of Alloys and Compounds, 886, (2021), 161130. https://doi.org/10.1016/j.jallcom.2021.161130.
3) C. Moise, L. Rachmani, G. Mihai, O. Lazar, M. Enăchescu, N. Naveh, Pulsed Laser Deposition of SWCNTs on Carbon Fibres: Effect of Deposition Temperature, Polymers, 13, (2021), 7, 1138. https://doi.org/10.3390/polym13071138
4) Ed. Monaico, C. Moise, G. Mihai, V. V. Ursaki, K. Leistner, I. M. Tiginyanu, M. Enachescu, K. Nielsch, Towards Uniform

Electrochemical Porosification of Bulk HVPE-Grown GaN, Journal of the Electrochemical Society, 166, (2019), 5, p. H3159-H3166. DOI: 10.1149/2.0251905jes

5) O.A. Lazar, C. C. Moise, A.S. Nikolov, L-B Enache, G.V. Mihai, M. Enachescu, The Water-Based Synthesis of Platinum Nanoparticles Using KrF Excimer Laser Ablation, Nanomaterials, 12, (2022), 3, 348 https://doi.org/10.3390/nano12030348

6) J. Sun A., Klechikov, C. Moise, M. Prodana, M. Enachescu, A. V. Talyzin "A Molecular Pillar Approach To Grow Vertical Covalent Organic Framework Nanosheets on Graphene: Hybrid Materials for Energy Storage." ANGEWANDTE CHEMIE-International Edition, 57, (2017), 4, p:1034-1038. DOI: 10.1002/anie.201710502

7) A. Marinoiu, I. Gatto, M. Raceanu, M. Varlam , C. Moise, A. Pantazi, C. Jianu, I. Stefanescu, M. Enachescu, Low cost iodine doped graphene for fuel cellelectrodes, International Journal of Hydrogen Energy, 42, (2017), 43, p. 26877-26888. DOI:10.1016/j.ijhydene.2017.07.036

8) J. Al-Zanganawee, M. AL-Timimi, A. Pantazi, O. Brîncoveanu, C. Moise, R. Mesterca, D. Balan, S. Iftimie, M. Enachescu, Morphological and optical properties of functionalized SWCNTs:P3OT nanocomposite thin films, prepared by spincoating, Journal of Ovonic Research, 12, (2016), 4, p. 201- 207.

9) J. Al-Zanganawee, T. Mubarak, A. Katona, C. Moise, D. Balan, D. Dorobantu, D. Bojin, M. Enachescu, Raman spectroscopy and morphology characterizations of SWCNTs synthesized by KrF excimer laser ablation under neon gas atmosphere, Digest Journal of Nanomaterials and Biostructures, 11, (2016), 2, p. 525-536.

10) J. Al-Zanganawee, A. Katona, C. Moise, D. Bojin, M. Enachescu, Krypton gas for high quality single wall carbon nanotubes synthesis by KrF excimer laser ablation, Journal of Nanomaterials (2015), Art Number 909072. DOI: 10.1155/2015/909072.

11) J. Al-Zanganawee, C. Moise, A. Katona, D. Bojin, M. Enachescu, Characterization of single wall carbon nanotubes synthesized by KrF excimer laser ablation in

nitrogen atmosphere, Digest Journal of Nanomaterials and Biostructures, 10, (2015), 4, p. 1119-1127.

12) O. V. Iaseniuc, M. S. Iovu, A. pantazi, O. A. lazar, <u>C. C. Moise</u>, M. enachescu, Assessing the structural properties of GexAsxSe1-2x chalcogenide systems through cross-correlated STEM, XRD and micro-Raman studies, Optoelectronics and Advanced Materials - Rapid Communications, 15, (2021), 9-10, pp.498-503.

13) S. P. Rosoiu, S. Costovici, <u>C. Moise</u>, A. Petica, L. Anicai, T. Visan, Marius Enachescu, Electrodeposition of ternary Sn-Cu-Ni alloys as lead-free solders using deep eutectic solvents, Electrochimica Acta, 398, (2021), 139339. doi.org/10.1016/j.electacta.2021.139339

14) L. Anicai, A. Petica, S. Costovici, <u>C. Moise</u>, O. Brincoveanu, T. Visan, Electrodeposition of Sn–In Alloys Involving Deep Eutectic Solvents, Coatings, 9, (2019),12, 800. https://doi.org/10.3390/coatings9120800

15) S. Inaba, R. Arai, G. Mihai, O. Lazar, <u>C. Moise</u>, M. Enachescu, Y. Takeoka, V. Vohra, Eco-Friendly Push-Coated Polymer Solar Cells with No Active Material Wastes Yield Power Conversion Efficiencies over 5.5%, ACS Applied Materials & Interfaces, Vol 11, (2019), 11, p. 10785-10793. DOI: 10.1021/acsami.8b22337

16) O.Brincoveanu, A. Ioanid, R. Mesterca, A.Pantazi, <u>C. Moise,</u> M. Enachescu, S.Iftimie, S. Antohe, "Glucose detection using BSA: PEDOT-PSS as bioactive solute and solid bioactive layer deposited by spin coating" Romanian Reports in Physics, 71, (2019), 2, art. No. 603.

17) A. Carac, R. Boscencu, R.M. Dinica, J. F. Guerreiro, F. Silva, F. Marques, M. P. Cabral Campello, <u>C. Moise,</u> O. Brincoveanu, M. Enachescu, G. Carac, A. Tabacaru, Synthesis, characterization and antitumor activity of two new dipyridinium ylide based lanthanide(III) complexes, Inorganica Chimica Acta, Vol 480, (2018), p. 83-90. DOI: 10.1016/j.ica.2018.05.003

BOOK CHAPTER ISI

18) C. Moise, and M. Enachescu, "High-Quality Carbon Nanomaterials Synthesized by Excimer Laser Ablation", in

Applications of Laser Ablation - Thin Film Deposition, Nanomaterial Synthesis and Surface Modification. London, United Kingdom: IntechOpen, 2016 [Online]. Available: https://www.intechopen.com/chapters/52517 doi: 10.5772/65309

NON ISI – During PhD

19) C. Moise, M. Enăchescu, Nanomateriale din carbon de calitate superioară sintetizate prin ablaţie cu excimer laser, Buletinul Societatii de Chimie Nr. XXIV 2/2016 p 15-39.

20) C. Moise, A. Pantazi, M. Enăchescu, CSSNT, un jucător cheie în rezolvarea "puzzle-urilor" din nanotehnologie, Buletinul Societății de Chimie din România Nr. XXVII, 1/2020 p 38-43.

OLD ISI PAPER OVERVIEW:

21) R.Ionescu, A.Vancu, C.Moise, A.Tomescu, Role of water vapours in the interaction of SnO2 gas sensors with CO and CH$_4$, Sensors and Actuators B, 61, 1999, 39-42. DOI: 10.1016/S09254005(99)00277-4

22) R. Ionescu, C. Moise, A. Vancu, Are modulations of the Schottky surface barrier the only explanation for the gas sensing effects in sintered SnO2 ?, Appl. Surf. Sci., 84, (1995), p. 291 – 297. DOI: 10.1016/0169-4332(94)00544-3

23) T. Yamanaka, Y. Ohno, A. Lesar, T. Matsushima, C. Moise, Studies on reaction site of carbon monoxide oxidation on platinum (113) by angle resolved thermal desorbtion, Surface Science, 357/358, (1996), 759-763. DOI: 10.1016/0039-6028(96)00259-2

24) T. Yamanaka, C. Moise and T. Matsushima, Reaction site switching in carbon monoxide oxidation on platinum (113); A spatial distribution study of desorbing products, Journal of Chemical Physics, 107, (1997), 8138-8146. DOI: 10.1063/1.475077

25) T. Yamanaka, Y. Inoue, M. Sano, C. Moise, T. Matsushima, Reaction sites of photo-induced carbon monoxide oxidation

on stepped platinum (113) surface, Appl. Surf. Sci., 121/122, (1997), 601 – 604. DOI: 10.1016/S0169-4332(97)00376-0

26) H. Akiyama, <u>C. Moise</u>, T. Yamanaka, K Jacobi, and T. Matshushima, Selective desactivation of reaction site for carbon monoxide oxidation on stepped platinum (113) surface, Chem. Phys. Lett., 272, (1997), 219-224. DOI: 10.1016/S0009-2614(97)88012-8.

OLD NON-ISI PUBLICATIONS:

27) T. Matsushima, <u>C. Moise</u>, T. Yamanaka "Identification of reaction sites for carbon monoxide oxidation on platinum metals", Trends in Chemical Physics (India) 4 (1996) 1-11 – **review paper**

28) T. Yamanaka, <u>C. Moise</u>, and T. Matsushima, Switching of reaction sites in catalytic oxidation of carbon monoxide on Pt(113), Catalysis (Japanese), 37 (1995) 438-441

29) <u>C.Moise</u>, R.Ionescu, A.Vancu, A.Tomescu, Influence of oxygen partial pressure on the kinetics of some physical parameters at transitions between dried and wet atmospheres in SnO2 gas sensors, Electron Technology, 33, (1999) ½, pp. (Poland)

TABLE IF, AIS and SRI PUBLISHED PAPER DURING PhD

Nr Lista	IMPACT FACTOR (IF)	1-st AUTHOR	ARTICLE INFLUENCE SCORE (AIS)	RELATIVE INFLUNCE SCORE (SRI)
1	2.881	X	0.376	0.999
2	5.316	X	0.719	1.471
3	4.329	X	0.599	0.925
4	3.721	X	0.715	1.899
5	5.076		0.759	1.687
6	12.257		3.241	8.736
7	4.43		0.57	1.206
8	0.698		0.109	0.259
9	0.836		0.15	0.34
10	1.758		0.411	0.917
11	0.756		0.139	0.309
12	0.441		0.062	0.148
13	6.901		0.944	1.616
14	2.436		0.376	0.999
15	8.758		1.686	3.641
16	2.147		0.269	0.614
17	2.3		0.272	0.84
18	UN CAPITOL DE CARTE	X		
TOTAL	65.041	5	11.397	26.606
	IMPACT FACTOR (IF)	1-st AUTHOR	ARTICLE INFLUENCE SCORE (AIS)	RELATIVE INFLUNCE SCORE (SRI)

INTERNATIONAL CONFERENCES
SELECTION -ORAL PRESENTATION

1. <u>C. Moise</u>, O. Brincoveanu, A. Katona, D. Dorobantu, D. Bojin, M. Enachescu "The study of *p*-Si/Al2O3/*n*-Si (100) sandwiches structures deposited by KrF excimer laser ablation" 40th ARA Congress 2016, Montreal, Canada.
2. <u>C. Moise</u>, D. Dorobantu, A. Pruna, M. Enachescu "Carbon nanomaterials for law enforcement clothing" Greener and Safer Energetic and Ballistic Systems - GSEBS 2016, București, România.
3. <u>C. Moise</u>, A. Jderu, A. Pantazi, R. Mesterca, D. Dorobantu, M. Enachescu „Innovative reactor for laser ablation synthesis of carbon nanomaterials" European Advanced Materials Congress, EAMC-2018, Stockholm, Sweden.
4. <u>C. Moise</u>, A. Jderu, A. Pantazi, R. Mesterca, D. Dorobantu, M. Enachescu *"Three Carbon Nanomaterials Synthesized by KrF Laser Ablation in an Innovative Reactor"* International conference CHIMIA 2018, NOMARES, Constanța, România.
5. G. Mihai, <u>C. Moise</u>, A. Pantazi, A. Jderu, O. Tutunaru, R. Meșterca, O. Lazăr, A. Pumnea, D. Dorobanțu, M. Enăchescu "Optimization of PMMA processing as a prerequisite for nanodevice building using Electron Beam Lithography" International conference CHIMIA 2018, NOMARES, Constanța, România
6. L. Anicai, S. Costovici, S. Rosoiu, <u>C. Moise</u>, T. Visan " Electrodeposition of Sn Based Ternary Alloys Using Deep Eutectic Solvents" 21st Romanian International Conference on Chemistry and Chemical Engineering RICCE 2019, Mamaia, România.
7. S. Rosoiu, S. Costovici, <u>C. Moise</u>, L. Anicai, T. Visan, M. Enachescu "Electrodeposition of ternary Sn-Cu-Ni alloys as lead-free solders using Deep Eutectic Solvents", Eurocorr 2020, Brussels, Belgia.
8. G. Mihai, <u>C. Moise</u>, O. Lazar, V. Anastasoaie, L. B. Enache, S. Rosoiu, M. Vardaki, A. Pantazi, M. Enachescu "GaN Nanostructuring" NOMARES 2020.
9. L. Anicai, A. Petica, A-C. Manea, <u>C. Moise</u>, T. Visan, *"Environmentally-Friendly Cerium-Based Conversion Coatings Obtained by Cathodic Electrodeposition in Deep*

Eutectic Solvents Formulations for Corrosion Protection of AA7075 Aluminium Alloys" **72nd Annual ISE Meeting** Jeju, Korea 29 August – 3 Septembrie 2021.

10. L. Anicai, A. Petica, S. Costovici, A. Cojocaru, <u>C. Moise</u>, S. Rosoiu, T. Visan, "*Cathodic electrodeposition of cerium-based conversion coatings using deep eutectic solvents formulations for corrosion protection of AA7075 aluminium alloys,* **keynote** la The 8[th]Regional Symposium on Electrochemistry of South-East Europe, RSE-SEE 8 Graz, Austria ,11-15 Iulie 2022.